2019-01-01

Structural And Sedimentological Analysis Of The Bear Canyon Conglomerate, Southeastern California: Implications For The Timing And Style Of Miocene Deformation Within The Eastern California Shear Zone

Garrett Goff
University of Texas at El Paso

Recommended Citation

Goff, Garrett, "Structural And Sedimentological Analysis Of The Bear Canyon Conglomerate, Southeastern California: Implications For The Timing And Style Of Miocene Deformation Within The Eastern California Shear Zone" (2019). *Open Access Theses & Dissertations*. 2858.
https://digitalcommons.utep.edu/open_etd/2858

STRUCTURAL AND SEDIMENTOLOGICAL ANALYSIS OF THE BEAR CANYON CONGLOMERATE, SOUTHEASTERN CALIFORNIA: IMPLICATIONS FOR THE TIMING AND STYLE OF MIOCENE DEFORMATION WITHIN THE EASTERN CALIFORNIA SHEAR ZONE

GARRETT GOFF

Master's Program in Geological Sciences

APPROVED:

Jason W. Ricketts, Ph.D., Chair

Terry L. Pavlis, Ph.D.

Andrew P. Barth, Ph.D.

Stephen L. Crites, Jr., Ph.D.
Dean of the Graduate School

STRUCTURAL AND SEDIMENTOLOGICAL ANALYSIS OF THE BEAR CANYON CONGLOMERATE, SOUTHEASTERN CALIFORNIA: IMPLICATIONS FOR THE TIMING AND STYLE OF MIOCENE DEFORMATION WITHIN THE EASTERN CALIFORNIA SHEAR ZONE

by

GARRETT GOFF, B.S.

THESIS

Presented to the Faculty of the Graduate School of
The University of Texas at El Paso
in Partial Fulfillment
of the Requirements
for the Degree of

MASTER OF SCIENCE

Department of Geological Sciences
THE UNIVERSITY OF TEXAS AT EL PASO
December 2019

Abstract

The region between Indian Pass and Picacho State Recreation Area (PSRA) in southeastern California records complex deformation related to the transition from a Paleogene convergent margin to a Neogene transform setting, although the timing and nature of youngest deformation in this region remains incompletely known. A 1.7 km-thick section of Miocene Bear Canyon conglomerate (BCC) was studied to constrain this young period of deformation. These rocks lie unconformably upon 23 Ma volcanic and epiclastic rocks and a Mesozoic metamorphic basement terrane. Near PSRA the BCC contains locally derived clasts and can be further subdivided into three unconformity-bounded sequences, referred to as sequences I, II, and III from oldest to youngest. At Indian Pass, the 9.45 ± 0.27 Ma basalts of Black Mountain are interstratified with the upper part of the BCC, though it was unknown how these relationships extend to PSRA where detailed mapping had established the stratigraphic architecture of this unit. The BCC itself has been internally faulted and folded and preserves a set of NW-striking dextral faults, a set of NE-striking sinistral faults, and the prominent EW-trending Copper Basin reverse fault.

This project builds upon previous results by investigating BCC subdivision and provenance, continued mapping south of the Copper Basin fault and west of where the fault becomes elusive. These key details and their relation to the basalts of Black Mountain support and rectify gaps in existing studies.-Initial results suggest that east-west extensional stresses ceased ~17 Ma and were replaced by north-south shortening ~10-12 Ma. Sequence I of the BCC was deposited between 23 and 9.45 Ma, prior to deposition of the basalts of Black Mountain. These basalts lie between sequence II and III of the BCC. Sequence III near PSRA preserves numerous

faults and folds, which appear to record north-south contraction. These observations suggest that the BCC records onset of deformation related to development of the San Andreas transform margin.

Table of Contents

List of Figures

List of Tables

Introduction

Picacho State Recreation Area (PSRA) lies in southeastern California, approximately 26 miles north of Yuma, Arizona near the Arizona-California border in the southern extent of the Eastern California Shear Zone and just south of the Colorado River (Fig. 1). The Chocolate Mountains anticlinorium passes directly through the study area and is responsible for much of its recent development. Ricketts et al. (2011) built on past work in the area by detailing clast types and compositions of the Bear Canyon conglomerate (BCC) and dividing it into three sequences. Other authors have studied the local volcanic rocks (Needy et al., 2007; Biggs, 2008; Sainsbury, 2010; Sutton, 2010), basement complex (Jacobson et al., 1996, 2007), structure and timing (Muela, 2011), and implications for the Colorado River (Beard et al., 2016). These studies served as a base to investigate the youngest deformation event in the BCC by expanding the map area to the south.

There are several questions of interest in this study. 1) Are the basalts of Black Mountain interstratified with Sequence II or Sequence III of the BCC? 2) How is deformation of the BCC characterized in the hanging wall of the Copper Basin fault? 3) How young is the deformation of the BCC? To address these questions, a thorough understanding of the sedimentological characteristics of the BCC and the styles of subsequent deformation recorded by the unit must be understood. In particular, this research focused on tracing the Copper Basin fault as it cuts different sequences of the BCC in order to understand its relationship to other major faults in the region, including the San Andreas fault, located approximately 30 km to the west.

Geologic Background

Geologic Units

Metamorphic Basement Units

The metamorphic basement complex is composed of the Upper Cretaceous to Paleogene Orocopia Schist, a Mesozoic orthogneiss unit, and the Jurassic Winterhaven Formation. The Orocopia Schist is an Upper Cretaceous-Paleogene quartzofeldspathic unit. Quartz, albite, oligoclase, biotite, and phengitic muscovite imply amphibolite-grade metamorphism (Jacobson et al., 2002), and the partial to complete replacement of biotite by chlorite indicates a retrograde metamorphic event. The Chocolate Mountains fault separates the Orocopia Schist from the overlying orthogneiss unit. This low-angle fault likely formed as a thrust <60-48 Ma (Simpson, 1990; Oyarzabal et al., 1997) but was reactivated as an extensional structure <22 Ma (Dillon et al., 1990; Simpson, 1990; Jacobson et al., 2002; Yin, 2002).

The orthogneiss unit is composed of Jurassic and Cretaceous mylonitic middle- to upper-amphibolite facies rocks, indicated by high-Al hornblende and plagioclase, with centimeter-thick alternating mafic and felsic bands (Oyarzabal et al., 1997). Like in the Orocopia Schist, partial to complete replacement of biotite by chlorite throughout the area indicates a retrograde metamorphic event (Dillon et al., 1990; Simpson, 1990; Jacobson et al., 2002; Yin, 2002). This unit is then separated from overlying rocks by the 28-24 Ma Gatuna/Sortan fault , which was likely born a thrust fault but was reactivated as a normal fault like several other high-angle normal faults in the vicinity (Sainsbury, 2010).

The Winterhaven Formation is a greenschist facies unit that contains metavolcanic and metasedimentary rocks. It is structurally separated from the underlying orthogneiss unit by the

Gatuna/Sortan fault. The lower metavolcanic member is composed of aphanitic to porphyritic andesite to basalt with common penetrative fracturing (Sutton, 2010). The overlying metasedimentary member is composed of metamorphosed feldspathic and quartz arenite, argillite, and stretched-pebble conglomerate. The unit preserves bedding-parallel and anastomosing spaced cleavage throughout the area (Sainsbury, 2010; Sutton, 2010).

Volcanic Units

A thick pile of volcanic and volcaniclastic rocks lie unconformably on the metamorphic basement. This ~1.2 km section of rocks has been divided into seven separate units, and include from oldest to youngest the Quechan volcanic rocks, Marcus Wash rhyolite, Rojo Grande rhyolite, bedded pyroclastic and epiclastic rocks, White Wash rhyolite, ignimbrite of Ferguson Wash, and Walker volcanic rocks (Crowe, 1978; Sherrod and Tosdal, 1991; Biggs, 2008; Sainsbury, 2010; Sutton, 2010; Ricketts et al., 2011; Girty et al., 2012). Existing geochronology suggests that the stratigraphically lowest Quechan volcanics were deposited 23.4 ± 0.4 Ma and the stratigraphically highest unit, the ignimbrite of Ferguson Wash, was deposited 23.2 ± 0.2 Ma (Needy et al., 2007). Since these rocks were all deposited within such a short time frame and are not the focus of this study, these units are described below simply as a volcanic complex (Figs. 2, 3, Plate 1). However, as described below, the individual volcanic units are important because clasts derived from them are preserved in the overlying BCC, so a basic description of each unit is provided to aid in field identification.

The Quechan volcanics are a widespread, map-scale unit and the lowermost unit in the stratigraphic column. Consisting of basaltic to andesitic lava flows, flow breccia, and lahars, the Quechan volcanics range from basalt to trachyte in composition (Olson, 2010).

The Rojo Grande and Marcus Wash rhyolites occupy the same stratigraphic position directly above the Quechan volcanics. The White Wash rhyolite overlays the Rojo Grande rhyolite and appears to be interstratified with the widespread bedded pyroclastic and epiclastic flows in the area. These flows overlay the three rhyolites and are themselves overlain by the ignimbrite of Ferguson Wash. These bedded pyroclastic and epiclastic units consist of thin- to thick-bedded lithic to lapilli tuff, a lahar bearing pebble- to cobble-sized volcanic clasts, and epiclastic volcanic and conglomerate (Biggs, 2008; Sainsbury, 2010; Sutton, 2010). Pyroclastic portions of this unit owe their pale green color to epidotization, though unaltered portions chemically resemble the overlying ignimbrite of Ferguson Wash (Biggs, 2008; Sainsbury, 2010; Sutton, 2010). Epiclastic zones are characterized by matrix-supported, rounder clasts throughout and light gray, 2 mm to 2 cm subangular volcanic clasts in a (sandy?) framework.

The ignimbrite of Ferguson Wash is a widespread unit composed of multiple flows that cooled synchronously. It varies from welded to non-welded (Crowe, 1978; Biggs, 2008; Sainsbury, 2010; Sutton, 2010), with the welded portion acting as a map-scale ridge-forming spine throughout the map area. The ash to lapilli tuff consists of pumice fragments foremost, phenocrysts of plagioclase, biotite, and iron oxides, with trace amounts of fresh glass. Non-welded zones contain lithic fragments and euhedral biotite phenocrysts 1 mm in size. This unit is a rhyolite in the TAS classification scheme (Biggs, 2008; Sainsbury, 2010; Sutton, 2010).

The youngest unit in the section, the Walker volcanics, intrude into and through the bedded pyroclastics and epiclastics and the ignimbrite of Ferguson Wash. This generally andesitic unit is a greyish-red mix of plagioclase porphyry and flow breccia rich in feldspar phenocrysts in very fine-grained matrix. This unit is oxidized and altered by fluid in places as well (Biggs, 2008; Sainsbury, 2010; Sutton, 2010).

Bear Canyon Conglomerate

The BCC was deposited on the volcanic and epiclastic rocks along a pronounced angular unconformity. This unit contains several internal angular unconformities that led Girty et al. (2006) and Ricketts et al. (2011) to further subdivide the unit into three sequences, referred to as Sequences I, II, and III from oldest to youngest (Fig. 2). In addition, different facies within each sequence were identified, and these are referred to as members. Detailed mapping and lithologic descriptions of these sequences revealed distinctive clast compositions in each member (Ricketts et al., 2011). Sequence I is composed of member I, Sequence II is composed of members 2 and 3, and members 4-7 make up Sequence III.

Sequence I is a ~590 m thick unit consisting of paraconglomerate and orthoconglomerate containing clasts derived entirely from the underlying volcanic and volcaniclastic units (Girty et al., 2006; Ricketts et al., 2011). Within Sequence I, the percentage of clasts of Quechan volcanic rocks increases upward relative to clasts of the ignimbrite of Ferguson Wash. These observations suggest that Sequence I represents an unroofing sequence and was formed during the progressive dissection of the underlying volcanic units (Girty et al., 2006). The paraconglomerate beds are poorly sorted, medium- to thick-bedded, and usually inversely graded with pebble to boulder-sized clasts. The orthoconglomerates are thin-bedded, normally graded, and contain clasts no larger than pebbles (Ricketts et al., 2011).

Sequence II, totaling ~840 m thick, was deposited on Sequence I along a 5-10° angular unconformity. This unit contains clasts of the various underlying volcanic units as well as the metamorphic basement, and also features thin- to very thick-bedded polymictic paraconglomerates and orthoconglomerates (Ricketts et al., 2011). The lowermost section of Sequence II is Member 2, which is composed of orthoconglomerates that form tabular beds and

5-8 m wide and 1-2 m deep nested channels. Pebble- to cobble-sized clasts primarily fill these lenticular channels, though boulders are occasionally present. Member 2 is at times dominated by clasts from the Winterhaven Formation, while Member 3 is composed of volcanic clasts with rare basement clasts. These compositional differences are discussed later with clast count data. This member tends to be more organized, as it is comprised of well-sorted and subrounded to rounded pebble to cobble-sized clasts (Ricketts et al., 2011). To the south of the Copper Basin fault, Sequence II includes a distinctive gneiss-clast breccia (Fig. 3, 4; Plate 1) that interfingers with Member 2 (Fig. 5).

Sequences II and III are separated by a ~15° angular unconformity. Sequence III is ~440 m thick and is composed of thick- to very thick-bedded orthoconglomerates and paraconglomerates (Ricketts et al., 2011). Orthoconglomerates occasionally fill lenticular channels with cobble- to pebble-sized clasts, and medium- to thick-bedded paraconglomerates are less common throughout. Clasts in both types of conglomerate are poorly sorted, subangular, and derived from the underlying volcanic units and metamorphic basement, as well as farther-travelled clasts derived from units exposed to the south in the Cargo Muchacho Mountains. Member 4 is a well-sorted pebble- to boulder- orthoconglomerate. These angular clasts are derived almost entirely from the Orocopia Schist to the northwest as debris flows, similar as the gneiss-clast breccia in Sequence II. Member 5 is primarily an orthoconglomerate that is medium- to thick-bedded, poorly sorted, and forms lenticular and imbricated channels. A minor section of this member is a bedded, angular, and poorly sorted orthoconglomerate of debris flow origin. Member 6 is a very poorly sorted, thick-bedded paraconglomerate with clasts ranging from ~5 cm pebbles to 3+ m boulders. This unit is distinctive because it contains clasts of conglomerate with noticeable red staining. These clasts range in size from pebble to boulder and contain locally derived clasts of metamorphic basement and volcanic rock. Member 7 was previously denoted as part of Member 6, but it was subdivided because its clasts are derived from the nearby Cargo Muchacho Mountains rather than the local volcanic and metamorphic rocks. This unit is composed almost entirely of conglomerate with sub-angular to rounded pebble to cobble-sized clasts of kyanite- and dumortierite-rich felsic gneiss and rare volcanic clasts (Dillon and Ehlig, 1993).

Basalts of Black Mountain

The basalts of Black Mountain are exposed at Indian Pass and at Carrizo Wash (Plate 1). At Indian Pass the basalts are interstratified with the BCC, but it is unclear whether they are interstratified with Sequence II or Sequence III because this exposure has yet to be traced east where more-detailed mapping exists (Ricketts et al., 2011). Though the stratigraphic position of this exposure was elusive, $^{40}Ar/^{39}Ar$ isochron data from Muela (2011) shows the unit to be 9.45 ± 0.27 Ma. Another basalt exposure, originally mapped as part of the volcanic suite, is located near Carrizo Wash between Members 2, 4, and 5. This 9.69 ± 0.04 Ma (Ryan Crow, 2017, written communication) exposure is situated between Sequences II and III and shares a similar enough age with the Indian Pass location that this study classifies both exposures as the basalts of Black Mountain. At Indian Pass, the basalt is tilted south along the southern limb of the Chocolate Mountains anticlinorium, indicating that latest deformation occurred after the eruption of this unit (Ricketts et al., 2011).

Regional History

Formation of Metamorphic Basement

The Orocopia Schist is thought to have formed during the subduction of ocean sediments in the latest Cretaceous (Jacobson et al., 1996, 2007). During the Laramide Orogeny, low-angle east-dipping subduction entrained parts of the Franciscan Complex beneath the North American Plate. Normal faulting in this unit (Chocolate Mountains and Gatuna/Sortan faults) is most commonly associated with exhumation (Oyarzabal et al., 1997; Jacobson et al., 2007). The Chocolate Mountains fault, a younger feature than the Orocopia Mountains detachment system, was born a thrust but was reactivated ~ 52-50 Ma as an extensional detachment. ^{40}Ar/^{39}Ar thermochronologic data suggest that the < 60-44 Ma Chocolate Mountains fault and the 28-24 Ma Gatuna fault record two extensional pulses that exhumed the schist to near-surface levels in the crust (Jacobson et al., 2007). In addition to the Orocopia Schist, these faults exhumed the mafic orthogneiss and Winterhaven Formation. The Chocolate Mountains fault thrust this Jurassic(?) gneiss over the Late Cretaceous Orocopia Schist (Drobeck et al., 1986; Haxel et al., 1987; Dillon et al., 1990; Simpson, 1990; Oyarzabal et al., 1997; Jacobson et al., 2002). The Gatuna fault thrust the Jurassic(?) Winterhaven Formation over the orthogneiss. ^{40}Ar/^{39}Ar thermochronologic data in this unit suggest cooling in two events (Jacobson et al., 2002), the first of which is attributed to slip on the Gatuna fault (Jacobson et al., 2007).

Laramide Orogeny

The Farallon Plate began subducting beneath the North American Plate in the latest Jurassic period. Through the Cretaceous, continued subduction and arc magmatism developed the Sevier Orogen in the backarc (Ingersoll, 1997). Around 80 Ma, the subduction angle of the

Farallon Plate shallowed, marking the onset of the Laramide Orogeny. Flat-slab subduction sparked volcanism as far inland as eastern New Mexico, and thick-skinned deformation prevailed throughout western North America. This continued until ~40 Ma when part of the Farallon Plate broke off and the subduction angle steepened (Ingersoll, 1997).

Birth of the San Andreas Fault System

As Farallon Plate subduction continued, once again at a steep angle, the Mendocino Triple Junction (MTJ) and Rivera Triple Junction formed when the Farallon-Pacific ridge intersected the trench. No longer a typical subduction zone, coastal California was subjected to interactions with both the Farallon and Pacific Plates. The MTJ, the point at which these plates meet, complicates tectonic interactions (McKenzie and Morgan, 1969; Atwater, 1989; Ingersoll, 1997; Furlong and Schwartz, 2004). At ~28 Ma, the San Andreas fault formed to accommodate new tectonic stress in the region and changed the tectonic regime from a subduction zone to a transform margin. One result of triple junction interaction may have been the formation of a slab window (Fig. 6), a region where there is no underlying subducted oceanic lithosphere beneath continental lithosphere due to northward migration of the MTJ (McKenzie and Morgan, 1969; Furlong and Schwartz, 2004). The ~23 Ma volcanic rocks were deposited after the end of the Laramide Orogeny and during the initial growth of the San Andreas transform setting. There are several theories about the genesis of these volcanics since they are too far inland to fit a high angle subduction model, and they were erupted too late to be artifacts of Laramide volcanism. Olson (2010) investigated several of these, most of which discuss the validity of slab window crustal thinning as a volcanic driver. While slab window is generally credited for the widespread magmatism in the Cordillera, the igneous suite in the region between Indian Pass and PSRA is too felsic to fit the slab window model. Slab window-driven decompression melting produces

MORB- and OIB-like rocks by melting of peridotitic mantle, rather than the dacitic magmas produced further inland via crystal fractionation and magma mixing (Olson, 2010). Though numerous authors (Atwater, 1989; Richard, 1993; Needy et al., 2007; Muela, 2011; Bennett et al., 2016) have supported the slab window model as the driving force of magmatism in and around the Chocolate Mountains anticlinorium, geochemical data from the Quechan volcanic rocks (Olson, 2010) supports Dickinson's (2002) claim that slab window interaction was restricted to the immediate coastal vicinity of the Cordillera at 23 Ma.

Chocolate Mountains Anticlinorium

The Chocolate Mountains anticlinorium is a large anticlinal fold oblique to the San Andreas fault (Fig. 1). Just as the San Andreas fault's slip over time folded the BCC to the east, it also exhumed Mesozoic basement. Jacobson et al. (2007) analyzed several theories related to exhumation of the Pelona-Orocopia-Rand (POR) schist and the coincident formation of the Chocolate Mountains anticlinorium. They and other authors suggest that the anticlinorium initially formed as a consequence of exhumation of the POR schist, however the precise timing is debated (Yeats, 1968; Jacobson et al., 1996, 2002, 2007; Barth and Schneiderman, 1996; Wood and Saleeby, 1997; Ring and Brandon, 1999; Yin, 2002; Saleeby, 2003). Arc magmatism, driven by the decreased subduction angle of the Farallon plate in the Late Cretaceous, formed plutons further inland. The infant anticline had been uplifted sufficiently to interact with the upper crust. This growing tension was released with detachment faults, the Chocolate Mountains and Gatuna faults. Neogene transpression from the San Andreas fault further squeezed and tightened the Chocolate Mountains anticlinorium while transtensional features, such as the Salton Sea, formed further to the west (Jacobson et al., 2007).

Deposition and Deformation of the BCC

Ricketts et al. (2011) suggested that episodic Neogene growth of the Chocolate Mountains anticlinorium led to the three most significant angular unconformities. The ~ 30-60° E dip of the lower Miocene volcanic units is steeper than the overlying BCC, indicating some amount of anticlinorium development postdating eruption of the volcanic rocks and predates deposition of Sequence I. Similarly, Neogene fold growth is suggested by the deposition of Sequence II atop a folded Sequence I, creating a second angular unconformity. The second phase of fold growth began as Sequence II was folded along the anticlinorium's north and south limbs. Sequence III was deposited above the third unconformity, though fold growth continued in a third phase as Sequence III is also folded about the fold axis (Ricketts et al., 2011).

Neogene Structural Development

When the MTJ caused the subduction zone between the Pacific and North American Plates to transition into a near-vertical transform boundary, the Cordilleran margin was subjected to shearing stresses rather than compressional stresses (Atwater, 1989; Ingersoll, 1997; Furlong and Schwartz, 2004), with PSRA subjected primarily to extensional stress. Soon after the eruption of the ~23 Ma volcanic suite, Sequence I of the BCC was deposited on an angular unconformity. Folding in PSRA documents development of the Chocolate Mountains Anticlinorium. While the volcanic rocks dip ~ 30 – 60º, Sequence I dips ~21º. Folding continued episodically until at least ~9.45 Ma, after the deposition of the ~10 Ma basalts of Black Mountain (Ricketts et al., 2011). The loosely consolidated gravels overlying Sequence III dip <5º, while the alluvium lies flat.

Methods

This study was carried out in essentially three broad steps: 1) Geologic mapping in the field using the Chromebook, 2) sedimentological analysis of sequences II and III, including paleoflow orientations and clast compositions, in an effort to unravel the stratigraphic framework of the BCC in relation to the basalts of Black Mountain, and 3) structural analysis of faults and folds within Sequences II and III of the BCC.

This project resulted in a digitized and expanded geologic map of PSRA and revised stratigraphic framework based on the work of previous authors (Olson, 2010; Sainsbury, 2010; Sutton, 2010; Muela, 2011; Ricketts et al., 2011; Voyles, 2013). A compilation map that was the result of those authors' work served as the base for the expanded/revised map (Plate 1).

Traditional geologic field mapping gear was used in conjunction with digital mapping methods to collect data in the field. Field data was collected with a Brunton compass, a Garmin GLO Bluetooth GPS unit, and an ASUS Chromebook Flip C213SA with QGIS 2.8 *Wein* (used due to availability in the Lennox repository at the time of setup). The Chromebook was able to dual-boot with Linux Ubuntu in addition to the default Chrome OS. This modification allowed use of the QField Android application for field mapping, which was chosen for its simplified interface to remove potential error when adding points and lines on the map. QGIS 2.8 was used to revise the map at the end of each field day as well as to use a Google Earth layer that QField cannot currently handle. QGIS 2.18 *Las Palmas*, Google Earth 10.13.6, and Stereonet 9.9.3 (Allmendinger et al., 2012; Cardozo and Allmendinger, 2013) and FaultKin 8 (Marrett and Allmendinger, 1990; Allmendinger et al., 2012) were used for off-site processing and analysis.

This project resulted in several products, including a geologic map (Plate 1) that has been digitized, expanded, and simplified from an unpublished geologic map. A cross-section (Fig. 4) across the Copper Basin fault was constructed to supplement the new mapping to the south. For exposed faults in the study area, fault plane and slickenline (Fig. 7) orientations were measured, and sense-of-slip criteria were determined. Common slip sense indicators include Reidel shears, chatter marks, clast smear (Fig. 8) and ductile drag folds in the damage zone. Clast counts (Fig. 9 – 11, Table 1) and maximum BCC clast sizes (Fig. 12, Table 2) were compiled and plotted on the map. For each site, a total of 100 clasts ranging from 1-15 cm in diameter were identified and counted. Familiarity with the distinguishing characteristics of the metamorphic basement and volcanic rocks, as described below, aided in clast identification. Clast compositions are displayed on pie charts to highlight the compositional differences in each sequence of the BCC (Fig. 9 – 11, Table 1). Where visible, the maximum size of clasts of conglomerate in Sequence III were measured. Kinematic analyses for each style of fault (Fig. 13 – 15, Table 3) were combined with stereonet data to assess local and regional slip sense. These data were combined with data collected from Ricketts et al. (2011) to identify possible source(s) of conglomerate clasts in Sequence III.

Results

The overall map area extends from Indian Pass in the west to PSRA in the east. Within this region, more detailed mapping focused on a smaller area between Bear Canyon and Carrizo Wash in the central map area (Fig. 3). The axial trace of the Chocolate Mountains anticlinorium trends approximately EW and consists of a series of culminations and depressions. Culminations in the hingeline of the anticlinorium are present near Indian Pass and PSRA resulting in exposures of the metamorphic basement. A depression in the anticlinorium is present near the central mapping area in and near to Bear Canyon. Volcanic units dominate the east end of the map. The BCC was deposited in the central and southern portions of the map area and fills the depression in the anticlinorium. Sequence I is exposed to the north where Bear Canyon drains into the Colorado River. Sequence II is a widespread unit exposed in the central map area. Sequence III covers the most central part of the BCC and extends south along the southern edge of the metamorphic basement. Basement rocks, volcanics, and all three sequences of the BCC are cut by a series of NW-striking dextral and NE-striking sinistral strike-slip faults in the study area (Ricketts et al., 2011). Extending in an EW direction along the southern margin of the study area, the southward-dipping Copper Basin fault also cuts the entire package of rocks and shows reverse sense of slip (Sutton, 2010). In particular, near Bear Canyon the Copper Basin fault places mafic orthogneiss to the south structurally above Sequence III in the northern fault block. Further sedimentological and structural aspects of the BCC are described below in greater detail.

Sequences II and III dominate the southern portion of the map and are separated by the Copper Basin fault. Member 6's schist clasts in the foot wall are overlain by a hanging wall of gneiss clast breccia, linking two outcrops of its constituent orthogneiss. West of the thrust fault's exposure, Members 2 and 4 share a jagged contact before giving way to Member 7's distinctive milky white clasts. Tight synclines and small-scale faults are abundant on either side of the Copper Basin fault and diminish in amplitude away from the fault.

Sedimentological Analysis

Sequence I Clast Counts

Clast counts (Table 1) from the central map area were completed in order to identify any possible trends in composition within each of the three sequences and to use as criteria for subdividing the different members. Clast counts from Sequence I (Fig. 9) suggest that this unit is derived entirely from the underlying volcanic section; no clasts of metamorphic basement were observed (Girty et al., 2006). In addition, the relative abundance of clasts derived from the ignimbrite of Ferguson Wash increases up section, while the relative abundance of clasts derived from the Quechan volcanic rocks decreases, suggesting that Sequence I represents an unroofing sequence of the underlying volcanic section (Girty et al., 2006; Ricketts et al., 2011).

Sequence II Clast Counts

Sequence II (Fig. 10) records continued unroofing in the area, as it contains clasts of ~23 Ma volcanics and an assortment of clasts derived from the metamorphic basement. Member 2 ranges from 25 – 99% volcanics and is dominated by clasts of either mafic orthogneiss or Winterhaven Formation depending on the location. Member 2 tends to be more enriched in Winterhaven clasts to the south and shows an increase in gneiss clasts to the north.

Member 3 is dominated by volcanic clasts with rare metamorphic clasts. In the most southeasterly site, sample C88 contains no identifiable metamorphic clasts. In this regard Member 3 is very similar to Member 1, but Member 3 can be distinguished because it still contains up to 5% metamorphic clasts.

A gneiss-clast breccia is preserved to the south of the Copper Basin fault. Clast count results from two separate locations indicate a clast population that is approximately 87% gneiss and 13% schist. This unit is only present in proximity to the Copper Basin fault and was only measured in one location.

Sequence III Clast Counts

Member 4, exposed north of the Copper Basin fault, is composed mostly of conglomerate with clasts derived from the Orocopia Schist, with a maximum of 11% gneiss clasts. Gneiss clast abundance increases to the north and diminishes toward the fault's surface trace. Though more widespread in exposure, Member 4's clast composition is complimentary to that of Sequence II's gneiss-clast breccia.

Member 5 is dominated by gneiss clasts in the south and the west but gradually transitions toward a primarily volcanic clast composition in the northeast. Clasts of schist are rare or absent in the central extent of the member. This unit also contains clasts of a preexisting conglomerate. These conglomerate clasts themselves contain clasts derived from the local metamorphic and volcanic rocks. In Member 5, clasts of conglomerate generally make up ≤12% of the total assemblage.

Member 6 contains the most conglomerate clasts by far, though it is still dominated primarily by volcanic clasts. Clasts of gneiss dominate in most of the northwest extent. Winterhaven clasts can be found here in greater than trace amounts as well, likely due to close proximity with a Winterhaven exposure. In the northeast, BCC clasts make up 1/5 – 1/3 of the assemblage and even form a majority to the east (Fig. 11).

Member 7 also contains abundant clasts of gneiss. However, these clasts can be distinguished because they are more felsic in composition and not derived from the immediate exposures of mafic orthogneiss. The remaining clasts are generally volcanic; clasts derived from the metamorphic suite are a rarity. A singular clast count was collected, where 92% of the assemblage was felsic gneiss. These clasts dominate the unit throughout to give it its consistently milky color.

BCC Maximum Clast Diameters

Sequence III contains clasts of older BCC (Fig. 12) that vary greatly in size from boulders to pebbles. The largest observable clast in Sequence III, ~3m in diameter, is present in Member 5 near its boundary with Member 3. Maximum clast sizes in each outcrop generally decrease to the north and the west. In Carrizo Wash, the largest clast sizes are only 13 – 128 cm. It is likely that smaller clasts are present even farther west, but they would be unrecognizable if they eroded into their constituent clasts.

Basalts of Black Mountain

Based on previous mapping in and around Bear Canyon, the basalts of Black Mountain were known to be interstratified with either Sequence II or Sequence III of the BCC (Ricketts et al., 2011). At Indian Pass, this unit has a reported ^{40}Ar/^{39}Ar age of 9.45 ± 0.27 Ma (Muela, 2011). Ricketts et al. (2011) also mapped a separate sliver of basalt within Carrizo Wash that they assumed to be the 23.4 ± 0.4 Ma Quechan volcanics. However, a fresh sample was collected for geochronology, and the sample yielded a ^{40}Ar/^{39}Ar isochron age of 9.69 ± 0.04 Ma (Ryan Crow, 2017, written communication). Given this new age information, the basalt is correlated with the basalt at Indian Pass. The discovery of basalt of Black Mountain within Carrizo Wash has several implications. First, this basalt flow is not interstratified within either Sequence II or III. Rather, it was deposited between the two. As seen in Figure 3, the basalt lies above Member

2 of Sequence II, and is stratigraphically below Members 5 and 6 of Sequence III. This observation places tighter age constraints on the timing of deposition of Sequence II and Sequence III. Second, Ricketts et al. (2011) mapped a fault within Carrizo Wash. This fault was necessary to explain a sliver of Quechan volcanics interstratified within the BCC. However, given that this was the only compelling evidence for this fault, the fault has been removed in the updated map (Fig. 3, Plate 1).

Structural Analysis

In addition to understanding the stratigraphic architecture of the BCC, the second aspect of this research aimed to document key structures that cut these units. The BCC is internally faulted and folded, evidence for deformation younger than ~23 Ma, however the upper bound of this deformation is poorly constrained. In addition, a detailed kinematic analysis of minor faults within the BCC is lacking. Presented here are preliminary fault and slickenline data from the study area that are used to further understand the styles of deformation in relation to more regional tectonic patterns.

The Copper Basin fault thrusts Member 2 of Sequence II above Member 4 of Sequence III (Fig. 4). Throughout the map area, a fault-parallel syncline is preserved in beds of the BCC in the immediate footwall of the Copper Basin fault. In addition, this fault splays in several locales but mostly maintains a single surface trace in the southern half of the map area. In the west, near the southwest gneiss exposure, the fault splays and cuts the Winterhaven Formation and the gneiss-clast breccia. These fault splays then merge farther to the west just before the fault either terminates or ceases to be exposed.

While there is ample evidence of the fault to the east such evidence becomes elusive in the far west where Member 7 either covers the fault contact or the fault terminates. Member 7 does not show faulting like the rest of Sequence III, so the Copper Basin fault is either covered or it terminates.

Numerous normal faults (Fig. 13) are observed in Carrizo Wash. These faults generally trend NNW and preserve mostly dip-slip slickenlines. Reverse faults (Fig. 14) cluster near the Copper Basin reverse fault. To the south of the fault, mafic orthogneiss and Winterhaven Formation are exposed. These units lie structurally above Sequence II of the BCC along a small strand of the Copper Basin fault that branches from the main fault. Observed reverse faults generally strike east-west and have dips that range from 30 to 75 degrees. Strike-slip faults (Fig. 15) in the study strike NW or NE and have subhorizontal slickenlines.

All three styles of faulting cut Sequence III or faults in Sequence III. The Copper Basin Fault is cut by strike-slip faults, and normal faults are likely synchronous with reverse faults. Slip directions for each style of faulting support a schematic summarizing the Late Miocene state of stress in the PSRA-Indian Pass area (Fig. 16). The schematic is based on field and map observations but turned out to be very similar to the slip described via kinematic analysis. The data in Figure 16 shows vertical compression and E-W extension based on orientations of primary, intermediate, and tertiary stresses. Vertical extension and N-S compression are expressed by a map-scale thrust fault and rampant normal faulting, which also facilitates E-W extension with the aid of NW- and NE-striking strike-slip faults. Kinematic analysis of each of the three styles of faulting show slip along measured fault planes, confirming the accuracy of field slip sense assessments. Thrust fault orientations (Fig. 14) seem to deviate most from the calculated slip direction, however this makes sense in context. Normal and strike-slip faults are generally consistent in their strike throughout the map area, though the Copper Basin fault bends and splays throughout the southern map area. Since this is the only major reverse fault in the area, a greater disparity between calculated slip direction and measured fault planes seems more appropriate.

Discussion

The primary goals of this project were to investigate the interstratification of the basalts of Black Mountain, investigate the hanging wall of the Copper Basin fault, and determine the age of youngest deformation of the BCC. The work of numerous authors (Jacobson et al., 1996, 2007; Needy et al., 2007; Biggs, 2008; Sainsbury, 2010; Sutton, 2010; Muela, 2011; Ricketts et al., 2011; Beard et al., 2016) facilitated these inquiries and the development of an expanded digital geologic map of region extending from PSRA to India Pass.

Prior to this investigation, the BCC had been divided clearly into three sequences and six members (Ricketts et al., 2011). The basement complex had been studied (Jacobson et al., 1996, 2007), the suite of volcanics had been organized (Needy et al., 2007; Biggs, 2008; Olson, 2010; Sainsbury, 2010; Sutton, 2010), and the basalts of Black Mountain had been radiometrically dated (Muela, 2011). The basalts of Black Mountain are key to understanding the temporal relationships between sequences in the BCC. Based on revised mapping and new geochronologic results, the basalts of Black Mountain are here interpreted to be younger than Sequence II and older than Sequence III. Since Sequence III contains abundant evidence of deformation, the age of youngest deformation of the BCC postdates the eruption of the 9.45 Ma basalt.

Clast diameters measured in Sequence III reach their maximum slightly east of the contact between Members 5 and 1. Clast diameters also decrease parallel to paleoflow measurements from Ricketts et al. (2011), suggesting that the source of Sequence III clasts lies to the east of Bear Canyon. A likely candidate for these clasts is Little Picacho Peak in the southern portion of the map area. Little Picacho Peak (Fig. 17) is composed of a base of volcanic rock that is overlain by Sequence II of the BCC. Here, clast compositions are very similar to the clast compositions in the conglomerate preserved in Sequence III, and the matrix contains a similar red staining. Since the peak is a topographic high to the east of the largest BCC clasts, it is possible that this area is the source of conglomerate clasts in Bear Canyon and the surrounding washes. The absence of Sequence I in this location (Plate 1) suggests that the peak has been a topographic high at least since ~23 Ma.

While it was previously unclear when the youngest deformation event occurred in the BCC, the stratigraphic location of the basalts of Black Mountain illuminates this timing. The youngest deformation event in PSRA is younger than ~9.45 Ma due to the stratigraphic location of the basalts of Black Mountain. While several fault networks cut Sequence II, only the western NW-striking dextral faults cut the ~9.69 Ma basalt at Indian Pass. The Copper Basin fault is the final major deformation event in the BCC, and it may serve to link older fault networks.

Beard et al. (2016) recently suggested that the Copper Basin fault should terminate west of the area covered by previous mapping. Referencing a network of left-stepping, NW-striking dextral faults, they hypothesized that the Copper Basin thrust fault acts as a transition zone between NW-striking dextral faults to the north and south. N-striking normal faults facilitate thinning north of the Copper Basin fault. This study continued mapping of these normal faults on a smaller scale and continued tracing the Copper Basin fault, which seems to die out somewhere between exposures of gneiss-clast breccia and Member 7. Apparent termination of the Copper Basin fault (Fig. 3, Plate 1) and orientation of normal faults (Fig. 13) in the study area both support the local tectonic model proposed by Beard et al. (2016). Figure 16, which summarizes map-scale strain and deformation based on fault slip data, is also compatible with their model.

Deformation in the Eastern California Shear Zone has been ongoing through the Miocene, however this project and findings from Beard et al. (2016) may mean that development of the Chocolate Mountains anticlinorium may be younger than previously known. This study shows that the Copper Basin fault is younger than ~9.45 Ma, and cross-cutting strike-slip faults are younger still. Based on faults mapped south and west of PSRA-Indian Pass and measured geomorphological evolution, Beard et al. (2016) suggest that anticlinorium development could have continued until at least <5 Ma. They note a network of left-stepping dextral faults cutting the Copper Basin fault. These terminate roughly in the same location as the Copper Basin fault before giving way to a network of sinistral faults to the NW. This larger system of faults strongly resembles the faults mapped in this project. These studies together are evidence that deformation in the Eastern California Shear Zone continued <9.45 Ma, possibly <5 Ma, and that the Copper Basin Fault acts as a transition zone for left-stepping dextral faults in an environment shaped primarily by N-S shortening and E-W extension.

Conclusions

The geologic history of the PSRA-Indian Pass region spans at least ~60 Ma. While its early history has been more thoroughly investigated, the more recent events remained somewhat elusive. Numerous authors have previously determined deposition and deformation from the Late Cretaceous until the Miocene to be episodic in nature, but the finale of Neogene activity remained unknown without stratigraphic knowledge of the basalts of Black Mountain and the gneiss clast breccia near the Copper Basin fault. Recent geochronologic work revealed very similar ages of both basalt exposures, and these units' stratigraphic locations now serve as evidence that brittle deformation in PSRA-Indian Pass continued episodically from ~23 Ma until after at least ~9.45 Ma. One fault zone (Fig. 18) in the far south of the region, near Little Picacho Peak, remains enigmatic. It is unclear how and when a landslide block of Winterhaven Formation could become lodged intact between volcanic units. Questions, findings, and digital map resources from this study will hopefully serve future workers endeavoring to learn more about recent deformation in southern California and slip patterns in the San Andreas fault system.

References

Allmendinger, R.W., Cardozo, N., and Fisher, D.M., 2012, Structural geology algorithms: vectors and tensors: Cambridge ; New York, Cambridge University Press, 289 p.

Atwater, T., 1989, Plate tectonic history of the northeast Pacific and western North America: The Geology of North America, v. N, p. 55–72.

Barth, A.P., and Schneiderman, J.S., 1996, A Comparison of Structures in the Andean Orogen of Northern Chile and Exhumed Midcrustal Structures in Southern California, USA: An Analogy in Tectonic Style? International Geology Review, v. 38, p. 1075–1085, doi:10.1080/00206819709465383.

Beard, L.S., Haxel, G.B., Dorsey, R.J., McDougall, K.A., and Jacobson, C.E., 2016, Late Neogene deformation of the Chocolate Mountains Anticlinorium: implications for deposition of the Bouse Formation and early evolution of the Lower Colorado River: , p. 9.

Bennett, S.E.K., Darin, M.H., Dorsey, R.J., Skinner, L.A., and Umhoefer, P.J., 2016, Animated tectonic reconstruction of the Lower Colorado River region: implications for Late Miocene to Present deformation: , p. 15.

Biggs, M.A., 2008, Miocene volcanic rocks and conglomerates, SE California: evidence for Neogene reactivation of the Chocolate Mountains Anticlinorium: San Diego State University, 22 p.

Cardozo, N., and Allmendinger, R.W., 2013, Spherical projections with OSXStereonet: Computers & Geosciences, v. 51, p. 193–205, doi:10.1016/j.cageo.2012.07.021.

Crowe, B.M., 1978, Cenozoic volcanic geology and probable age of inception of basin-range faulting in the southeasternmost Chocolate Mountains, California: Geological Society of America Bulletin, v. 89, p. 251, doi:10.1130/0016-7606(1978)89<251:CVGAPA>2.0.CO;2.

Dickinson, W.R., 2002, The Basin and Range Province as a Composite Extensional Domain: International Geology Review, v. 44, p. 1–38, doi:10.2747/0020-6814.44.1.1.

Dillon, J.T., and Ehlig, P.L., 1993, Chapter 4: Displacement on the southern San Andreas fault, *in* Geological Society of America Memoirs The San Andreas Fault System: Displacement, Palinspastic Reconstruction, and Geologic Evolution, Geological Society of America, p. 199–216.

Dillon, J.T., Haxel, G.B., and Tosdal, R.M., 1990, Structural evidence for northeastward movement on the Chocolate Mountains Thrust, southeasternmost California: Journal of Geophysical Research, v. 95, p. 19953, doi:10.1029/JB095iB12p19953.

Drobeck, P.A., Hillemeyer, F.L., Frost, E.G., and Liebler, G.S., 1986, The Picacho Mine: a gold mineralized detachment in southeastern California, *in* Frontiers in geology and ore deposits of Arizona and the Southwest, Arizona Geological Society Digest, Tucson, Arizona Geological Society, v. 16, p. 187–221.

Furlong, K.P., and Schwartz, S.Y., 2004, INFLUENCE OF THE MENDOCINO TRIPLE JUNCTION ON THE TECTONICS OF COASTAL CALIFORNIA: Annual Review of Earth and Planetary Sciences, v. 32, p. 403–433, doi:10.1146/annurev.earth.32.101802.120252.

Girty, G.H. et al., 2006, Geology of the Picacho State Recreation Area, SE California: implications for the timing of formation of the Chocolate Mountains anticlinorium, *in* Using Stratigraphy Sedimentology, and Geochemistry to Unravel the Geologic History of the Southwestern Cordillera: A volume in honor of Patrick L. Abbot, Pacific Section, SEPM, v. 101, p. 77–96.

Girty, G.H. et al., 2012, Toward a unified model for the geologic and tectonic history of the region between Indian Pass and Picacho State Recreation Area, Southeastern California, *in* Picacho and the Cargo Muchachos, San Diego, California, San Diego Association of Geologists, p. 53–86.

Haxel, G.B., Budahn, J.R., Fries, T.L., King, B.W., White, L.D., Aruscavage, P.J., Dickinson, W.R., and Klute, M.A., 1987, Geochemistry of the Orocopia schist, southeastern California: summary, *in* Mesozoic rocks of southern Arizona and adjacent areas: Arizona Geological Society Digest, Arizona Geological Society, v. 18.

Ingersoll, R., 1997, Phanerozoic tectonic evolution of Central California and environs: International Geology Review, v. 39, p. 957–972.

Jacobson, C.E., Grove, M., Stamp, M.M., Vucic, A., Oyarzabal, F.R., Haxel, G.B., Tosdal, R.M., and Sherrod, D.R., 2002, Exhumation history of the Orocopia Schist and related rocks in the Gavilan Hills area of southeasternmost California, *in* Special Paper 365: Contributions to Crustal Evolution of the Southwestern United States, Geological Society of America, v. 365, p. 129–154, doi:10.1130/0-8137-2365-5.129.

Jacobson, C.E., Grove, M., Vućić, A., Pedrick, J.N., and Ebert, K.A., 2007, Exhumation of the Orocopia Schist and associated rocks of southeastern California: Relative roles of erosion, synsubduction tectonic denudation, and middle Cenozoic extension, *in* Special Paper 419: Convergent Margin Terranes and Associated Regions: A Tribute to W.G. Ernst, Geological Society of America, v. 419, p. 1–37, doi:10.1130/2007.2419(01).

Jacobson, C.E., Oyarzabal, F.R., and Haxel, G.B., 1996, Subduction and exhumation of the Pelona-Orocopia-Rand schists, southern California: Geology, v. 24, p. 547, doi:10.1130/0091-7613(1996)024<0547:SAEOTP>2.3.CO;2.

Lease, R.O., McQuarrie, N., Oskin, M., and Leier, A., 2009, Quantifying Dextral Shear on the Bristol-Granite Mountains Fault Zone: Successful Geologic Prediction from Kinematic

Compatibility of the Eastern California Shear Zone: The Journal of Geology, v. 117, p. 37–53, doi:10.1086/593320.

Marrett, R., and Allmendinger, R.W., 1990, Kinematic analysis of fault-slip data: Journal of Structural Geology, v. 12, p. 973–986, doi:10.1016/0191-8141(90)90093-E.

McKenzie, D.P., and Morgan, W.J., 1969, Evolution of triple junctions: Nature, v. 224, p. 125–133.

Muela, K.K., 2011, Timing and style of Miocene deformation, Indian Pass and Picacho State Recreation Area, SE California, U.S.A.: San Diego State University, 56 p.

Needy, S.K., Wooden, J.L., Barth, A.P., and Jacobson, C.E., 2007, Geochronology of igneous rocks in the Chocolate Mountains region as a means to interpret tectonic evolution of southeastern California:, https://gsa.confex.com/gsa/2007AM/finalprogram/abstract_124254.htm.

Olson, H., 2010, The early Miocene Quechan volcanics, SE California, U.S.A.: slab-window or continental-margin arc volcanics? San Diego State University, 56 p.

Oyarzabal, F.R., Jacobson, C.E., and Haxel, G.B., 1997, Extensional reactivation of the Chocolate Mountains subduction thrust in the Gavilan Hills of southeastern California: Tectonics, v. 16, p. 650–661, doi:10.1029/97TC01415.

Richard, S.M., 1993, Palinspastic reconstruction of southeastern California and southwestern Arizona for the Middle Miocene: Tectonics, v. 12, p. 830–854, doi:10.1029/92TC02951.

Ricketts, J.W., Girty, G.H., Sainsbury, J.S., Muela, K.K., Sutton, L.A., Biggs, M.A., and Voyles, E.M., 2011, Episodic growth of the Chocolate Mountains Anticlinorium recorded by the Neogene Bear Canyon Conglomerate, Southeastern California, U.S.A: Journal of Sedimentary Research, v. 81, p. 859–873, doi:10.2110/jsr.2011.66.

Ring, U., and Brandon, M.T., 1999, Ductile deformation and mass loss in the Franciscan Subduction Complex: implications for exhumation processes in accretionary wedges: Geological Society, London, Special Publications, v. 154, p. 55–86, doi:10.1144/GSL.SP.1999.154.01.03.

Sainsbury, J., 2010, Timing of extension, north-south shortening, and conjugate strike-slip faulting in the evolution of the Chocolate Mountains anticlinorium: Evidence from the Gavilan Hills, southeast California: San Diego State University, 42 p.

Saleeby, J., 2003, Segmentation of the Laramide Slab—evidence from the southern Sierra Nevada region: Geological Society of America Bulletin, v. 115, p. 655–668, doi:10.1130/0016-7606(2003)115<0655:SOTLSF>2.0.CO;2.

Simpson, C., 1990, Microstructural evidence for northeastward movement on the Chocolate Mountains Fault Zone, southeastern California: Journal of Geophysical Research, v. 95, p. 529, doi:10.1029/JB095iB01p00529.

Sutton, L., 2010, The Copper Basin fault, a newly recognized reverse fault in the lower Colorado River region, SE California: Implications for Miocene-Pliocene N-S shortening within the Eastern California Shear Zone: San Diego State University, 42 p.

Voyles, E., 2013, Assessing weathering intensity factors derived from sandy debris flow and sheet flood deposits of the Neogene Bear Canyon conglomerate, SE California, USA: San Diego State University, 65 p.

Wood, D.J., and Saleeby, J.B., 1997, Late Cretaceous-Paleocene Extensional Collapse and Disaggregation of the Southernmost Sierra Nevada Batholith: International Geology Review, v. 39, p. 973–1009, doi:10.1080/00206819709465314.

Yeats, R.S., 1968, Southern California Structure, Sea-Floor Spreading, and History of the Pacific Basin: Geological Society of America Bulletin, v. 79, p. 1693, doi:10.1130/0016-7606(1968)79[1693:SCSSSA]2.0.CO;2.

Yin, A., 2002, Passive-roof thrust model for the emplacement of the Pelona-Orocopia Schist in southern California, United States: Geology, v. 30, p. 183, doi:10.1130/0091-7613(2002)030<0183:PRTMFT>2.0.CO;2.

Figures

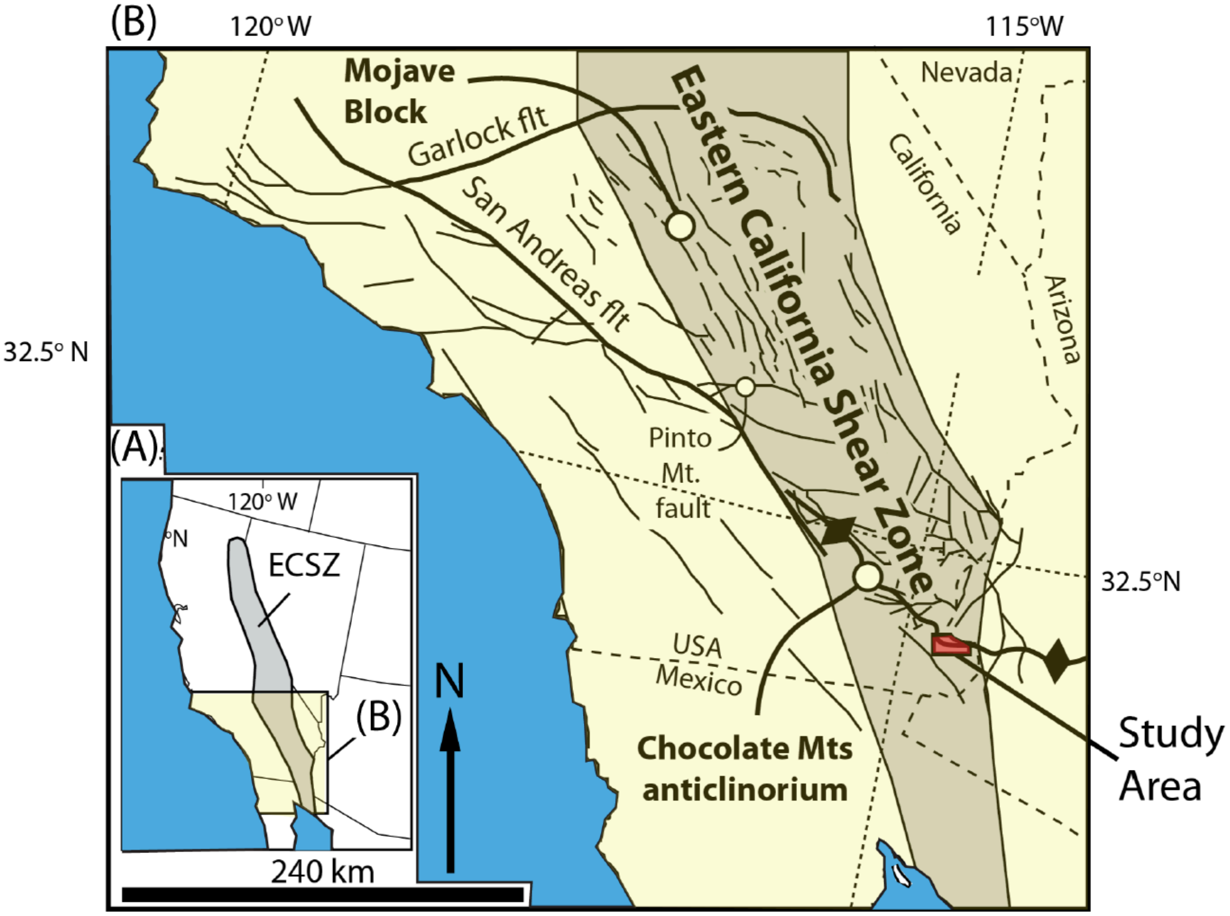

Figure 1. Zoomed-out view of study area, modified from Lease et al. (2009). Figure from Ricketts et al. (2011). The Eastern California Shear Zone is enclosed in the shaded polygon, and the Chocolate Mountains anticlinorium is denoted by the black line with diamonds. The study area is enclosed in the red polygon.

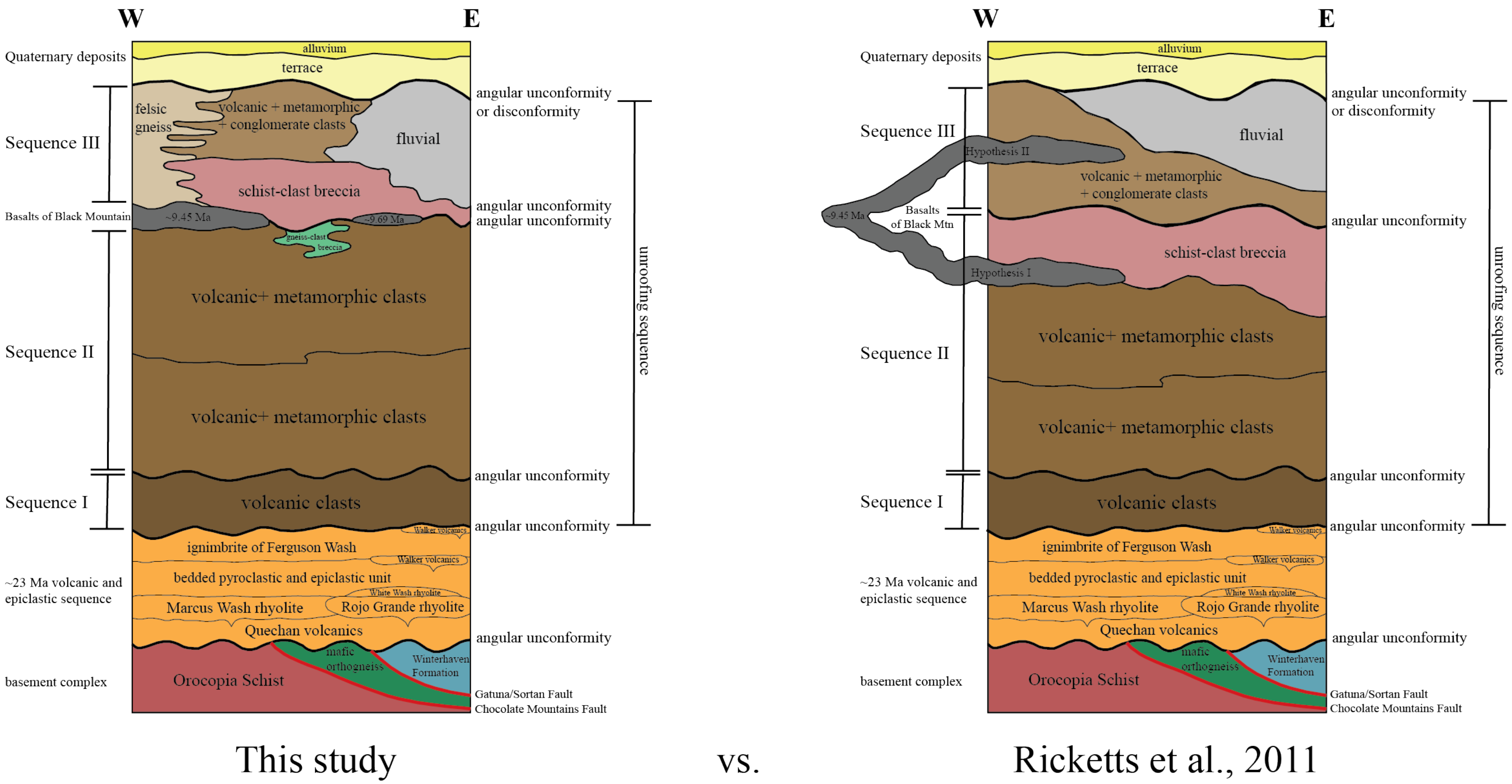

Figure 2. Regional stratigraphic columns for PSRA and Indian Pass area, color coordinated to match the geologic map (Fig. 3, Plate 1). The updated stratigraphic column produced by this study (left) is shown compared to that previously compiled (right) by Ricketts et al. (2011). Two hypotheses were considered in this study for the stratigraphic position of the basalts of Black Mountain. Neither of these were correct, however, as continued mapping revealed that the basalts lie between Sequences II and III.

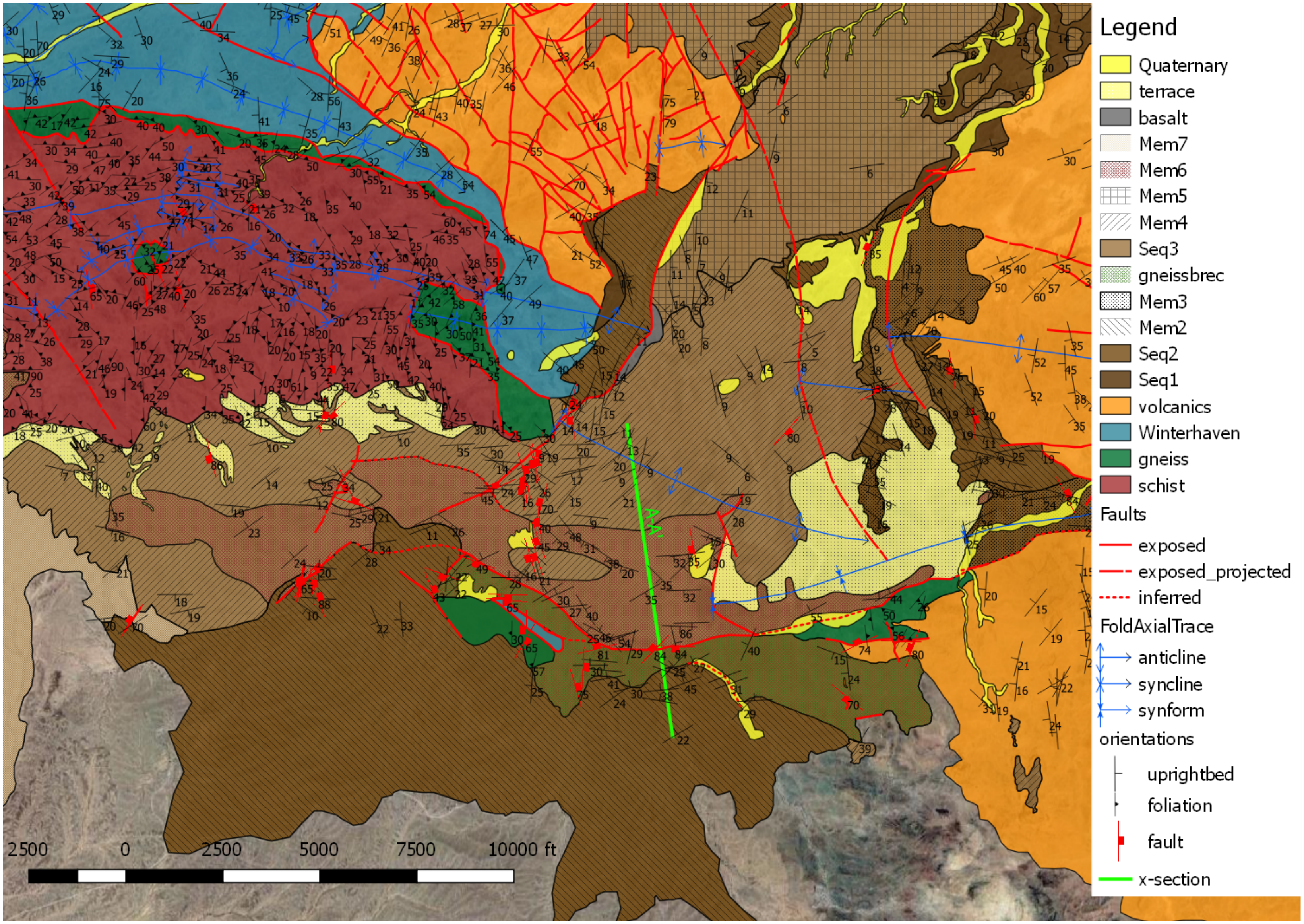

Figure 3. Geologic map of the study area, focused on the new area mapped. The full map is shown in Plate 1. The recently dated basalts of Black Mountain are represented by the small charcoal-colored unit north of center in this figure.

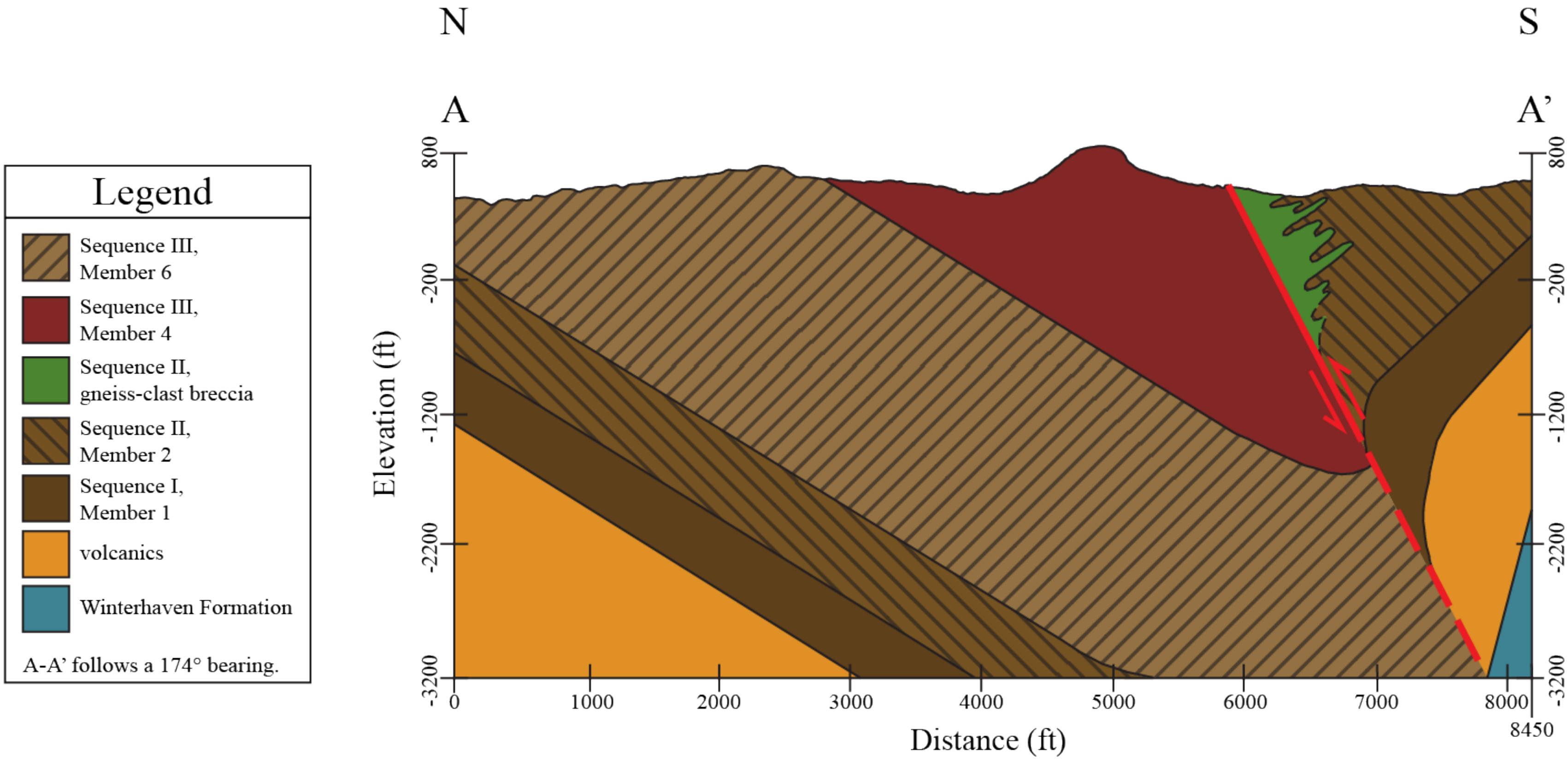

Figure 4. Cross section A-A’ across the Copper Basin fault in the southern map area. The gneiss-clast breccia is shown interfingering with Member 2 in the hanging wall. A-A’ is denoted by a lime green line in Plate 1.

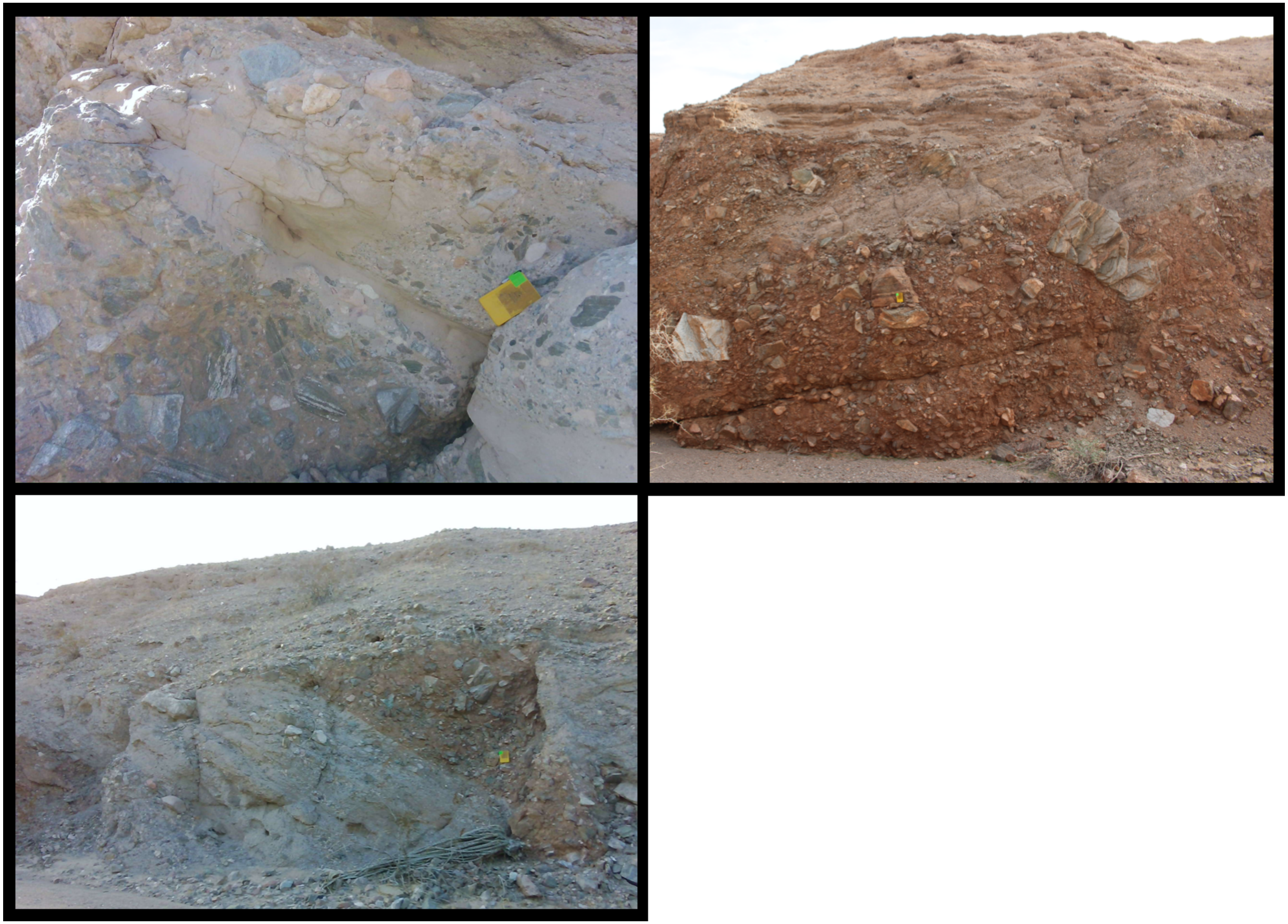

Figure 5. Gneiss-clast breccia interfingering with Member 2. These deposits lie south of the Copper Basin fault and adjacent to the mafic orthogneiss.

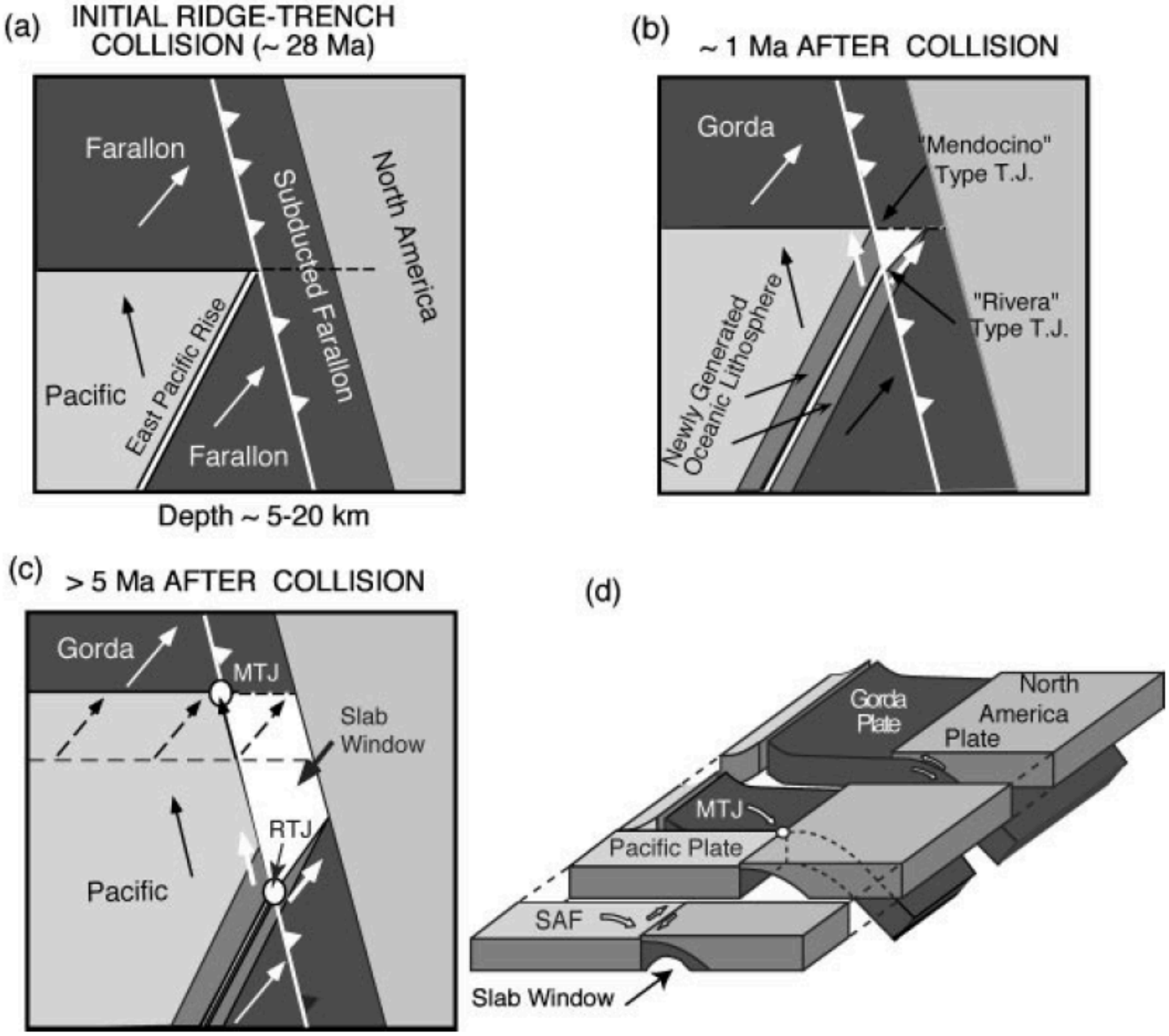

Figure 6. Formation and effects of slab window interaction with the North American plate between ~28 Ma and 23+ Ma. Figure from Furlong and Schwartz (2004).

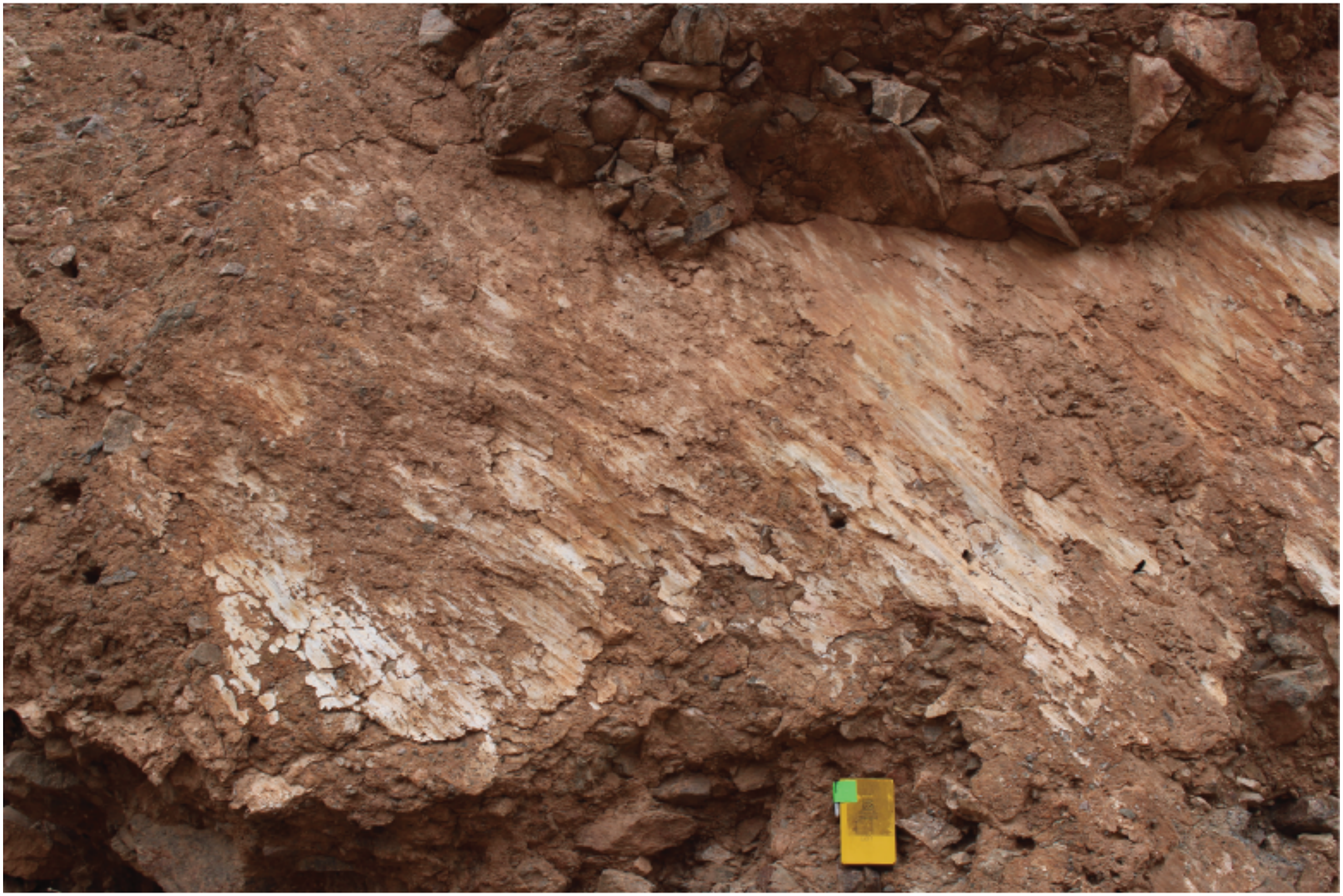

Figure 7. Dip-slip fault plane showing slickenlines used to measure rake and perform kinematic analysis.

Figure 8. Volcanic clast shown on a fault plane in Sequence II. The smear marks indicate slip and grinding of this clast along the plane and suggest dextral sense of motion.

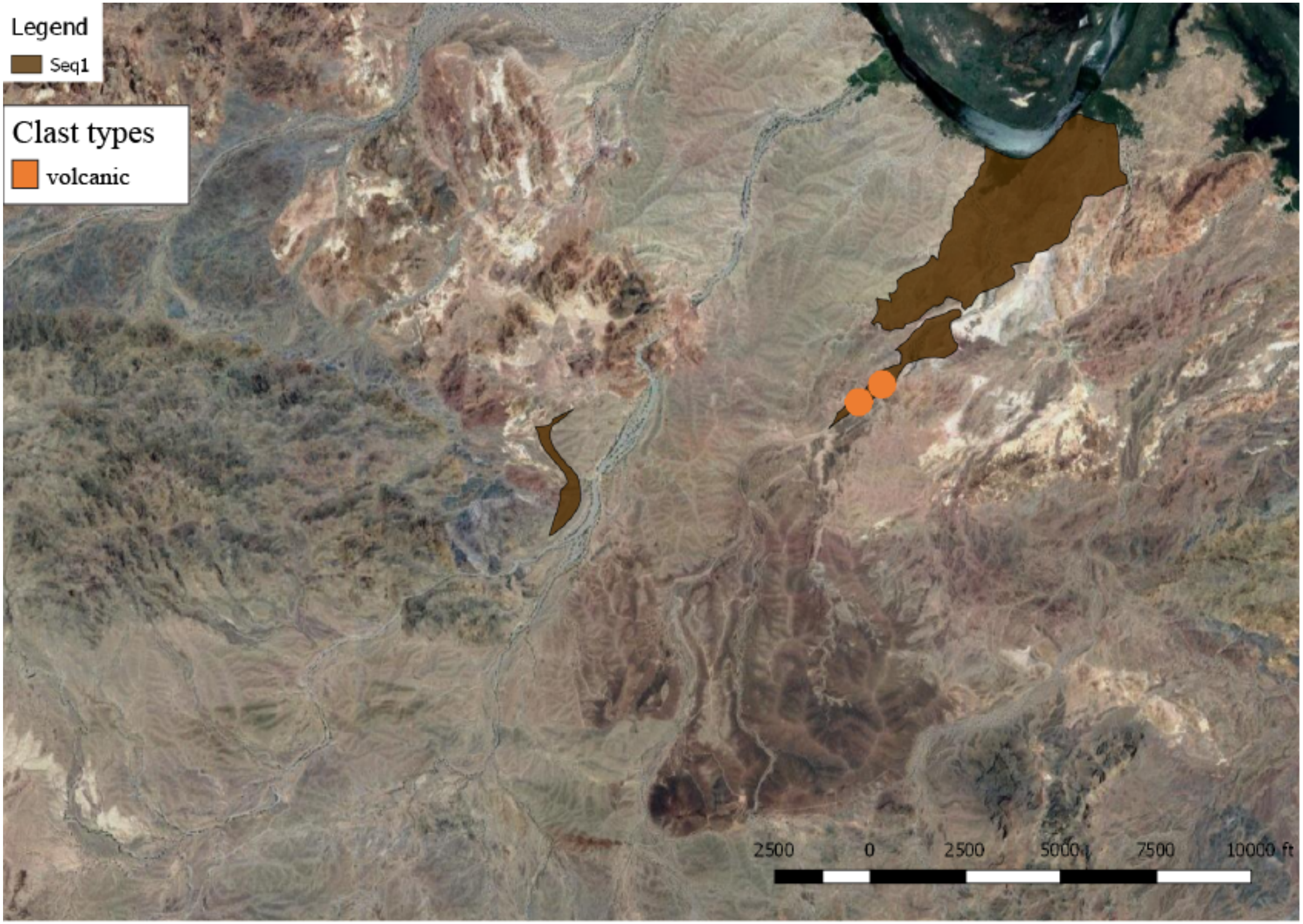

Figure 9. Map of clast counts in Sequence I. Sequence I is comprised solely of volcanic clasts and is synonymous with Member 1.

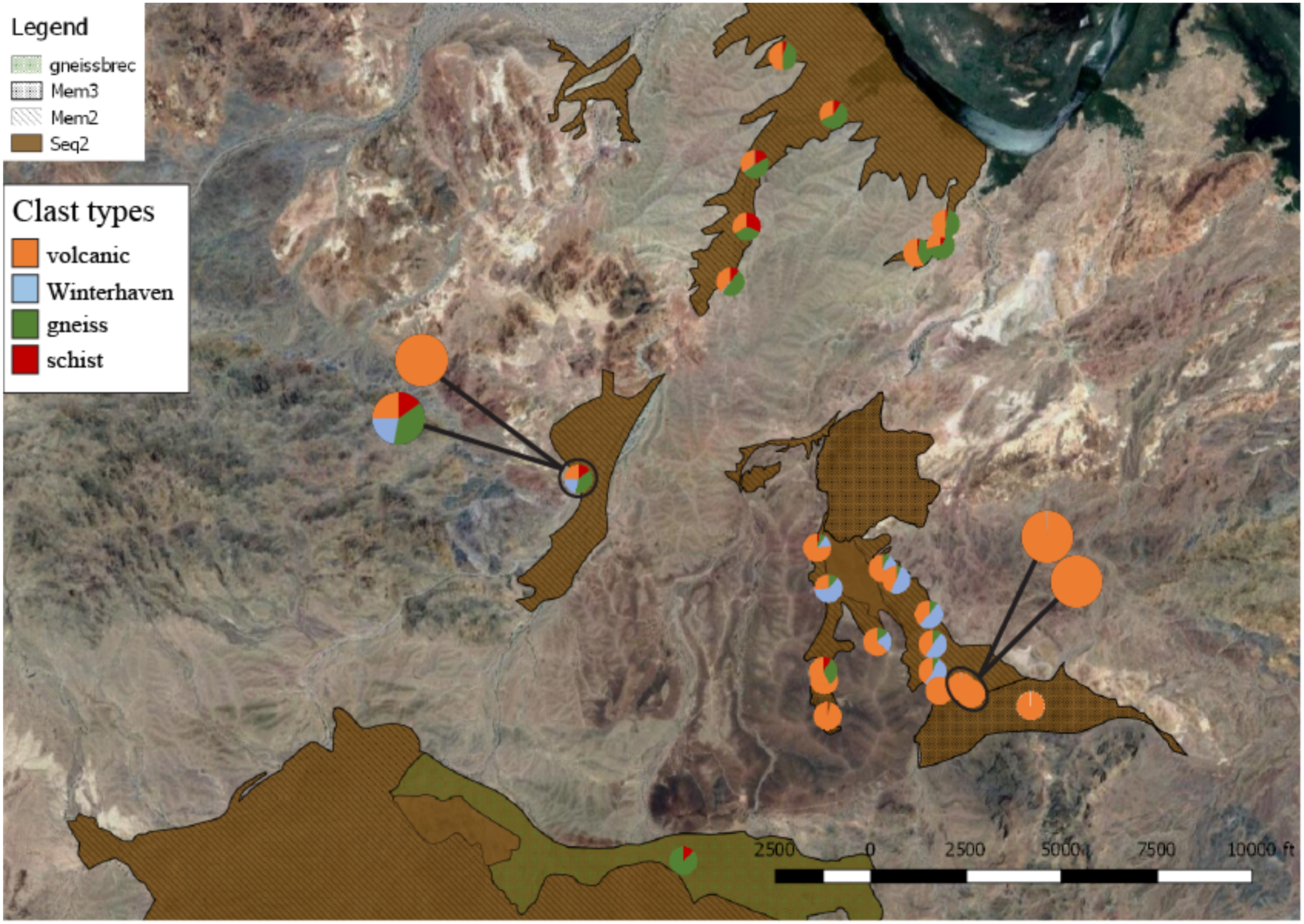

Figure 10. Map of clast counts in Sequence II. Sequence II is comprised of volcanic and metamorphic clasts and can be subdivided into Members 2 and 3 and a gneiss-clast breccia unit.

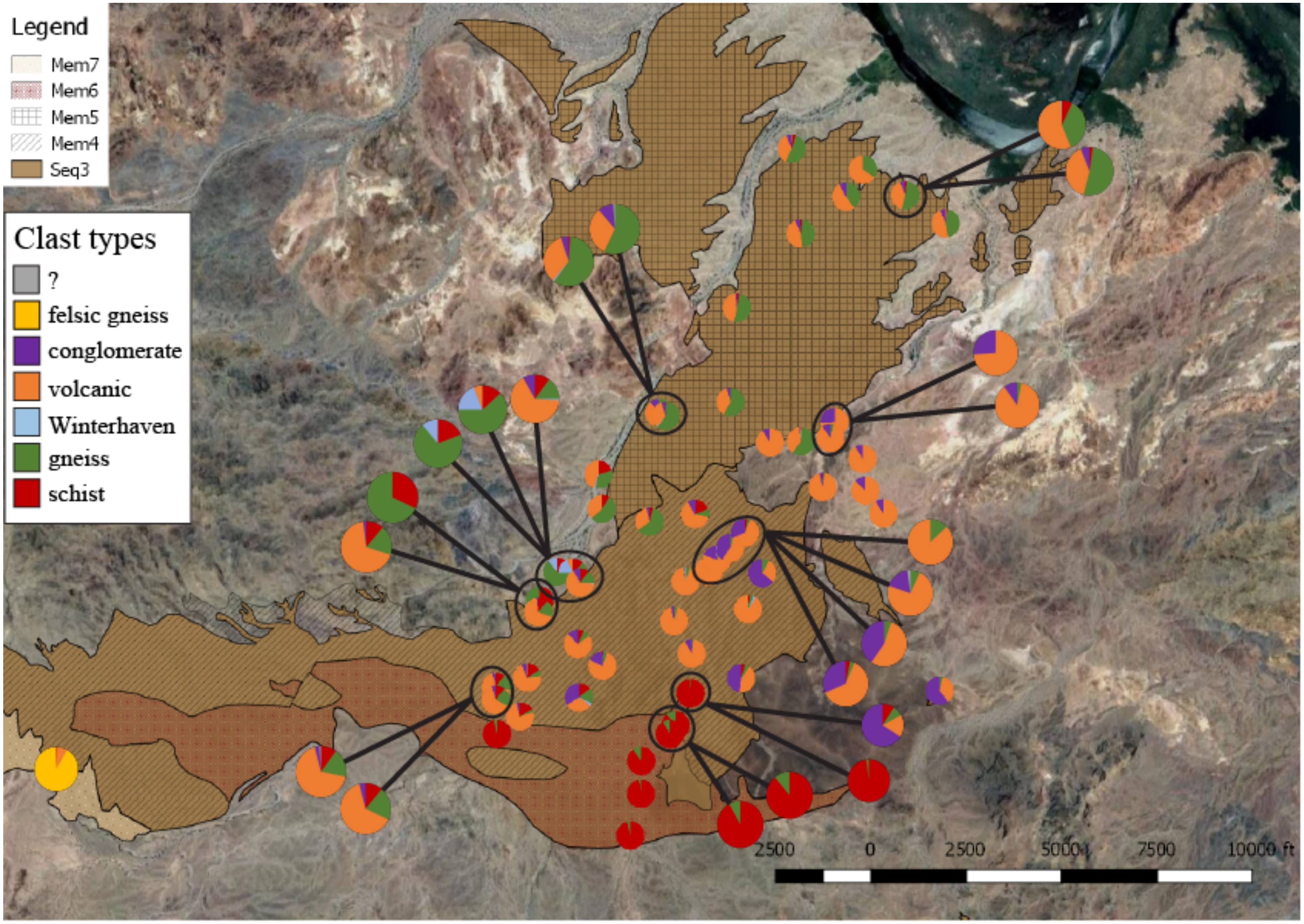

Figure 11. Map of clast counts in Sequence III. Sequence III is comprised of volcanic, metamorphic, and older conglomerate clasts and can be subdivided into Members 4, 5, and 6. Member 7 is shown in the far southwest with a singular clast count dominated by felsic gneiss content.

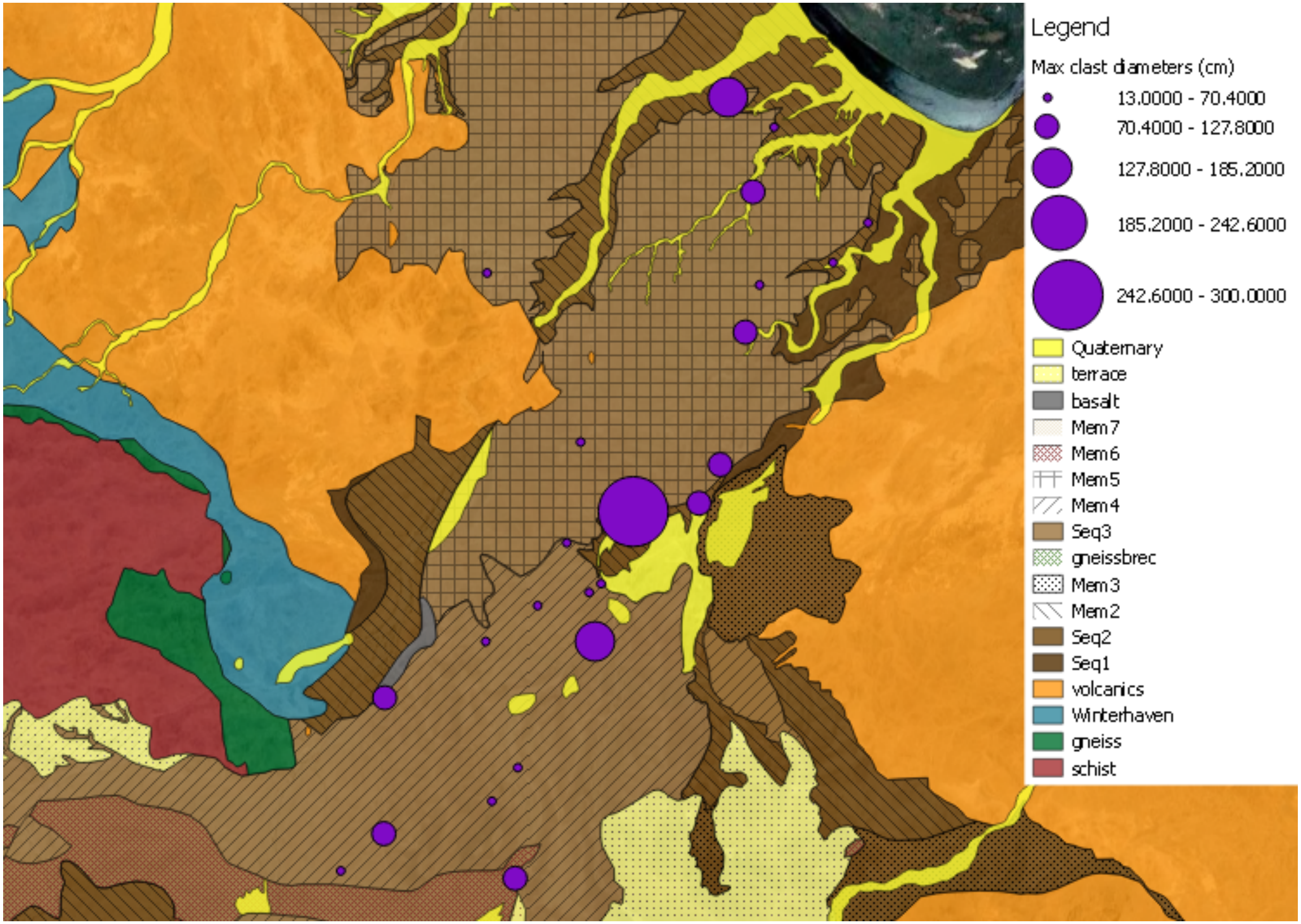

Figure 12. Maximum clast sizes of conglomerate in Sequence III found throughout Bear Canyon. Purple circles represent a range of clast sizes in cm, the largest of which is 300 cm in diameter.

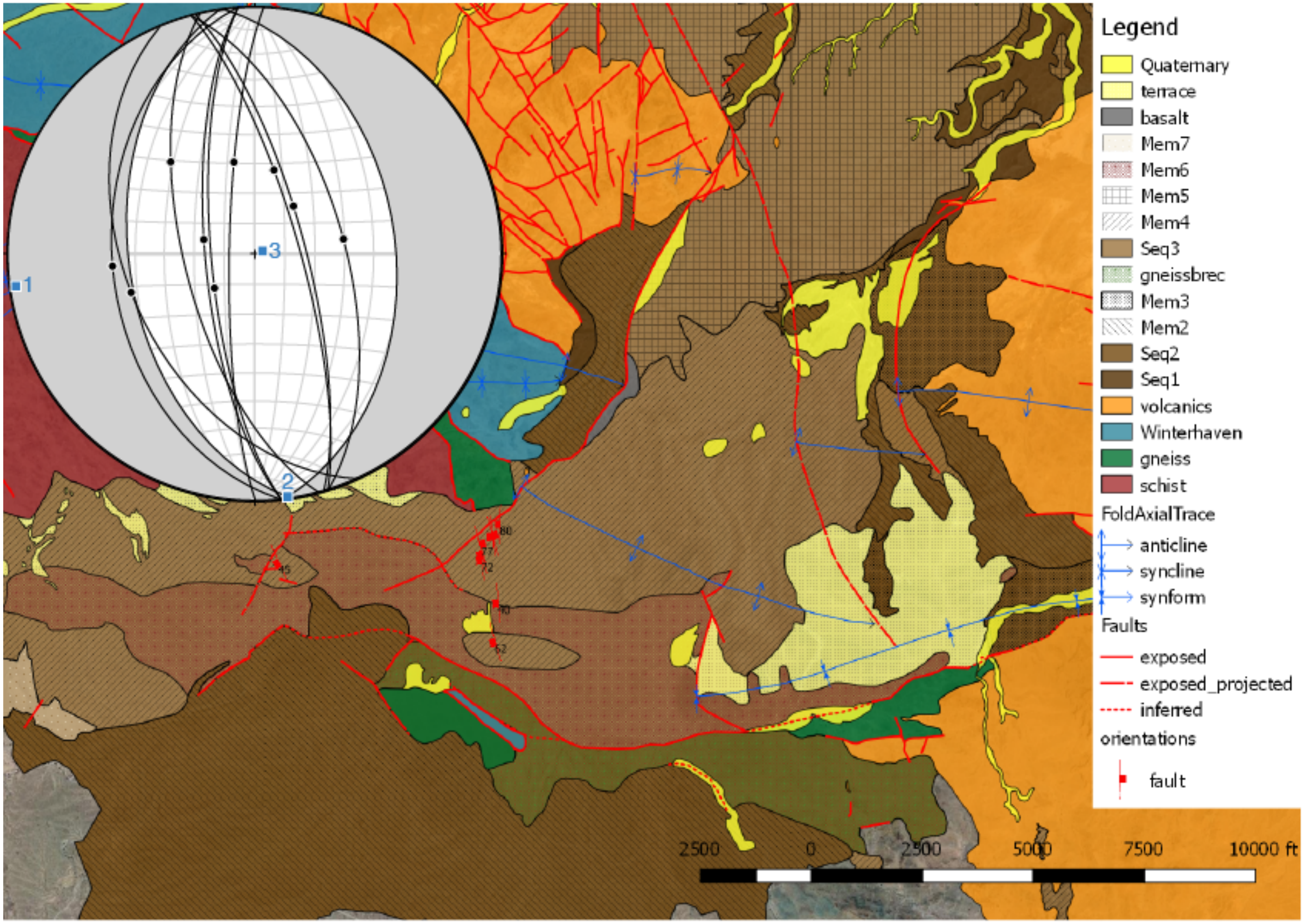

Figure 13. Map of normal faults measured in this study with combined stereonet overlaid. Only normal faults, shown in red, are plotted to the map. The overlaid chart includes poles to planes (shown as black dots) on which rake was measured, slip direction (shaded gray areas), and calculated stress field (shown as blue squares) for normal fault data.

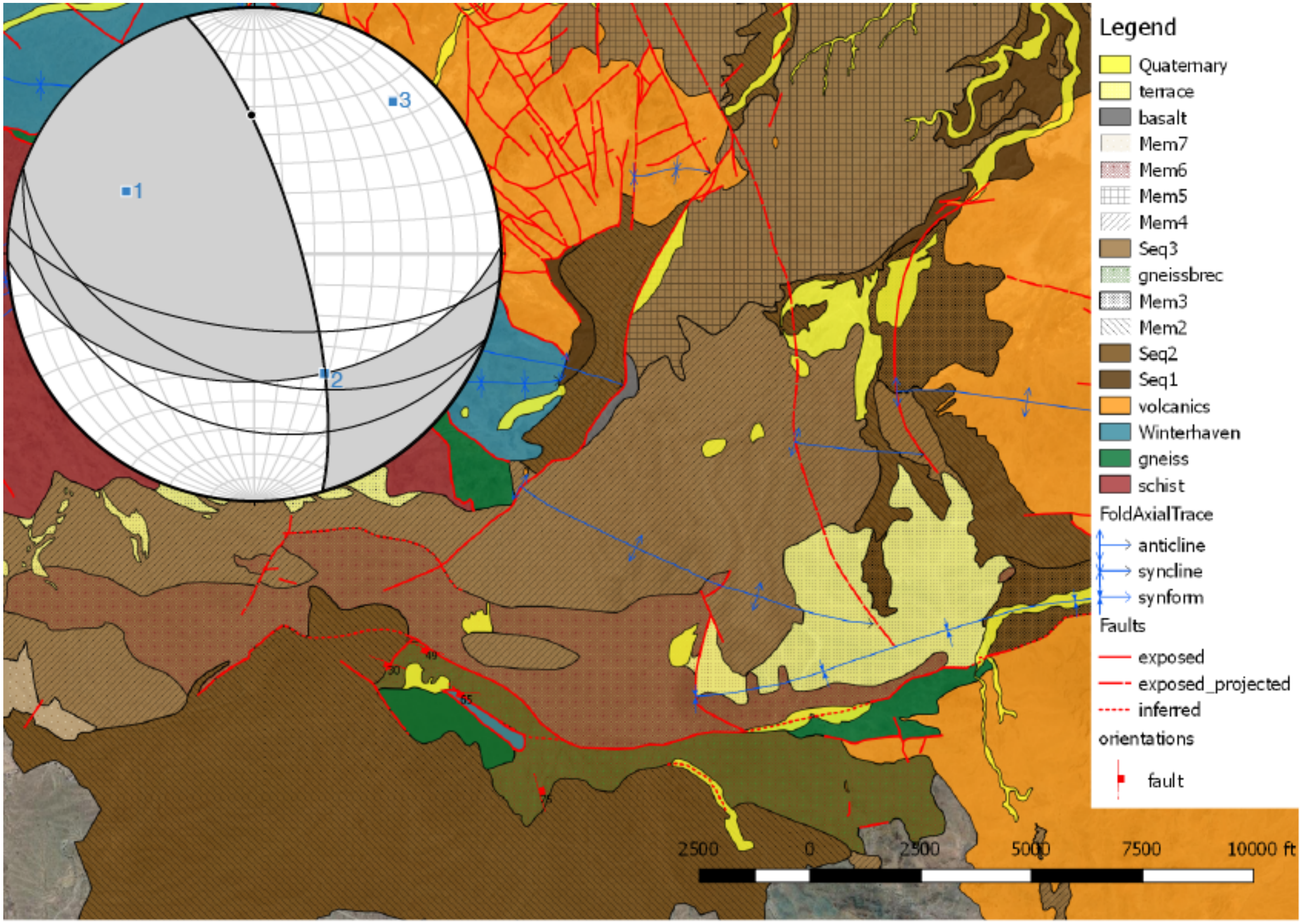

Figure 14. Map of reverse faults measured in this study with combined stereonet/focal mechanism overlaid. Only reverse faults, shown in red, are plotted to the map. The overlaid chart includes poles to planes (shown as black dots) on which rake was measured, slip direction (shaded gray areas), and calculated stress field (shown as blue squares) for reverse fault data.

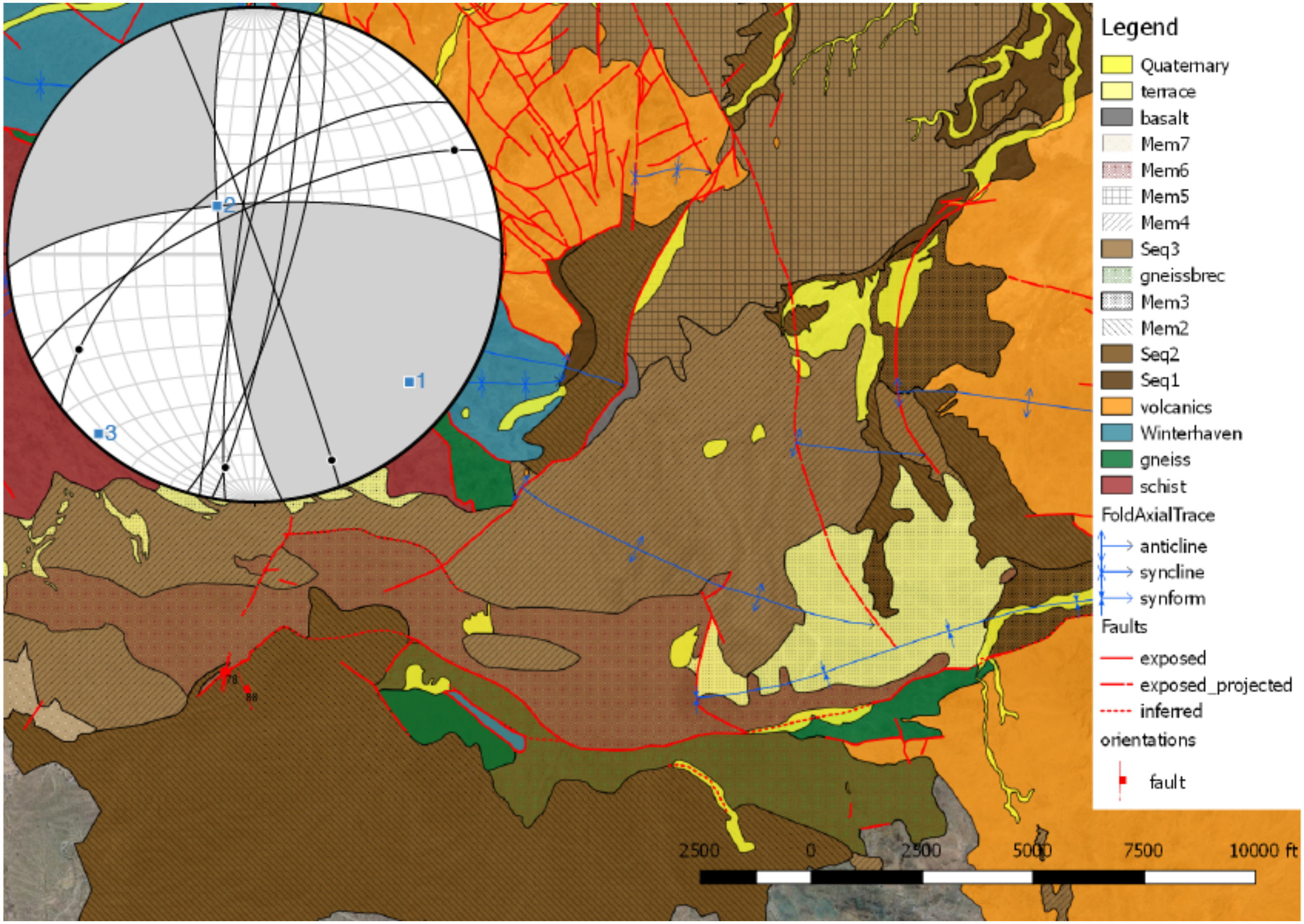

Figure 15. Map of strike-slip faults measured in this study with combined stereonet/focal mechanism overlaid. Only strike-slip faults, shown in red, are plotted to the map. The overlaid chart includes poles to planes (show as black dots) on which rake was measured, slip direction (shaded gray areas), and calculated stress field (shown as blue squares) for strike-slip fault data.

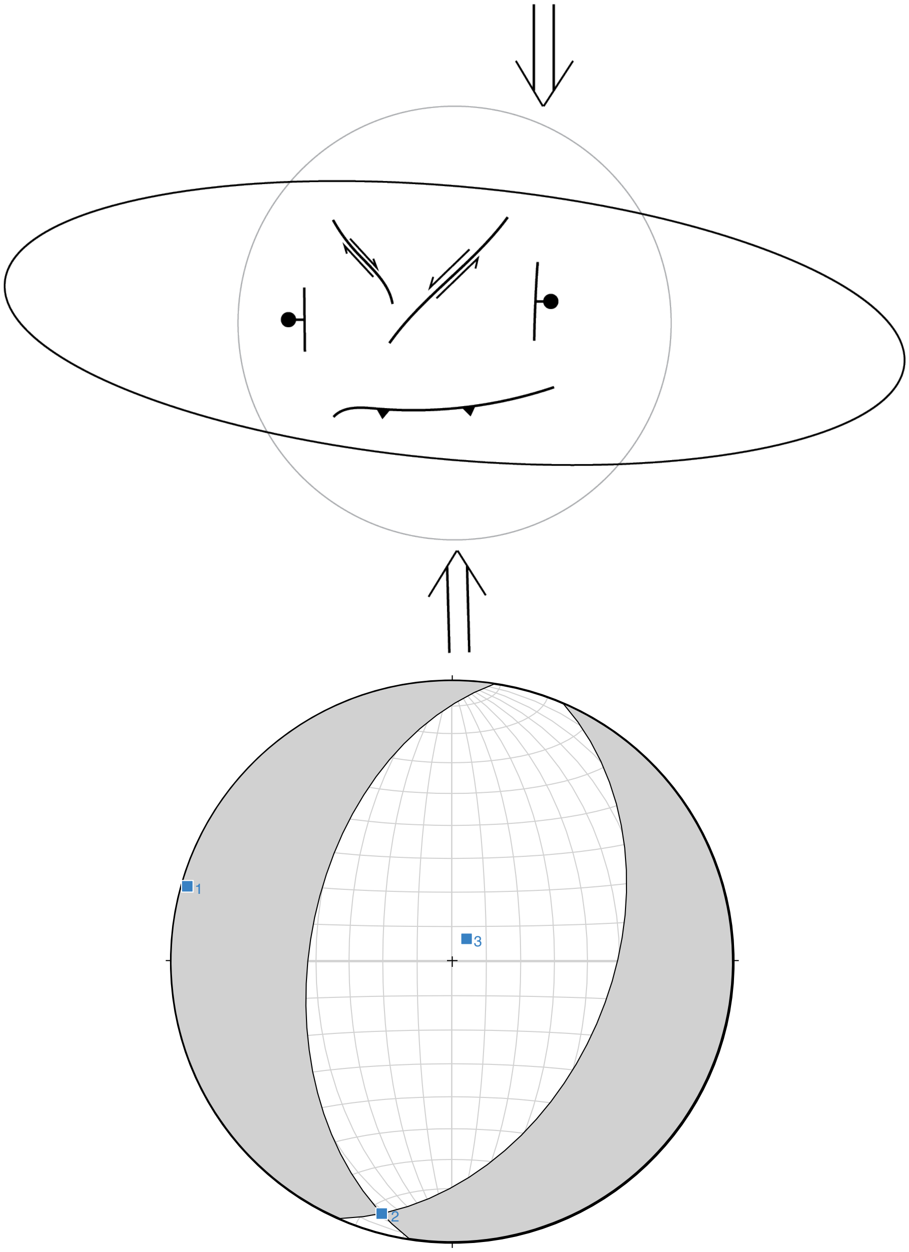

*Figure 16. Above: stress ellipsoid for PSRA showing N-S shortening and E-W extension facilitated by normal, reverse, and strike-slip faults, shown with approximate orientations. Below**:** focal mechanism calculated using all faults with rake measurements from this study. Blue squares show directions of primary, intermediate, and least stress according to slip of the faults.*

Figure 17. Little Picacho Peak, shown from its west face, shows Sequence II lying unconformably above the ~23 Ma volcanic complex.

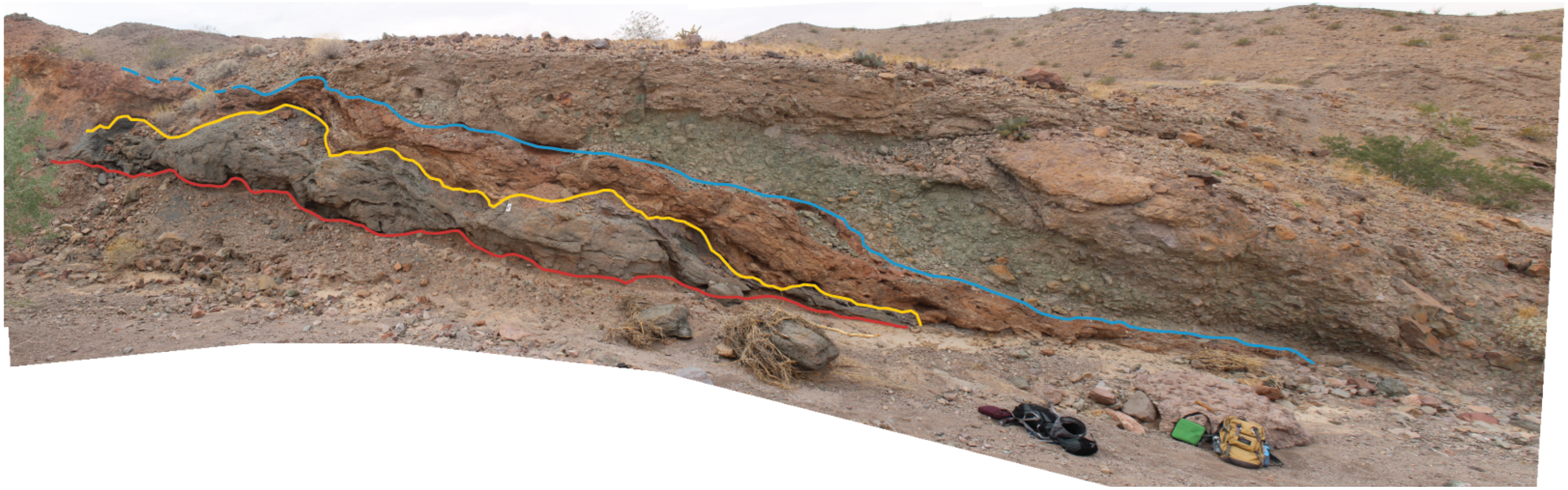

Figure 18. Panorama of a peculiar fault zone where a slab of the Winterhaven Formation (grey-blue, above red line) lies faulted between younger volcanic rock (rust brown, above yellow line) with fault breccia zones above (green, above blue line) and possibly below (subsurface, not shown). A tan 40-liter backpack is shown at the bottom right for scale.

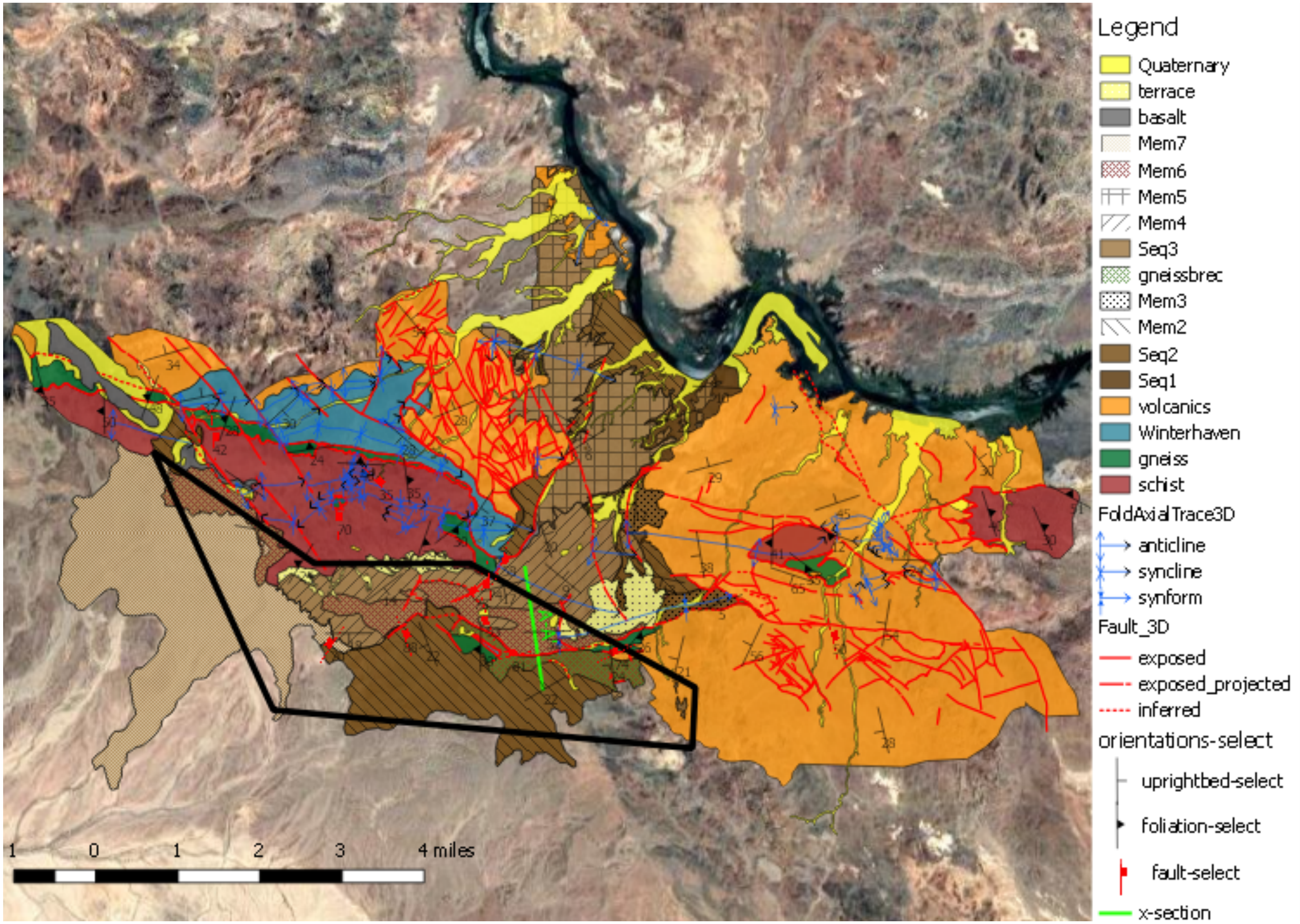

Plate 1. Geologic map of PSRA and Indian Pass. The polygon encloses roughly the new area that this project added to the compilation map.

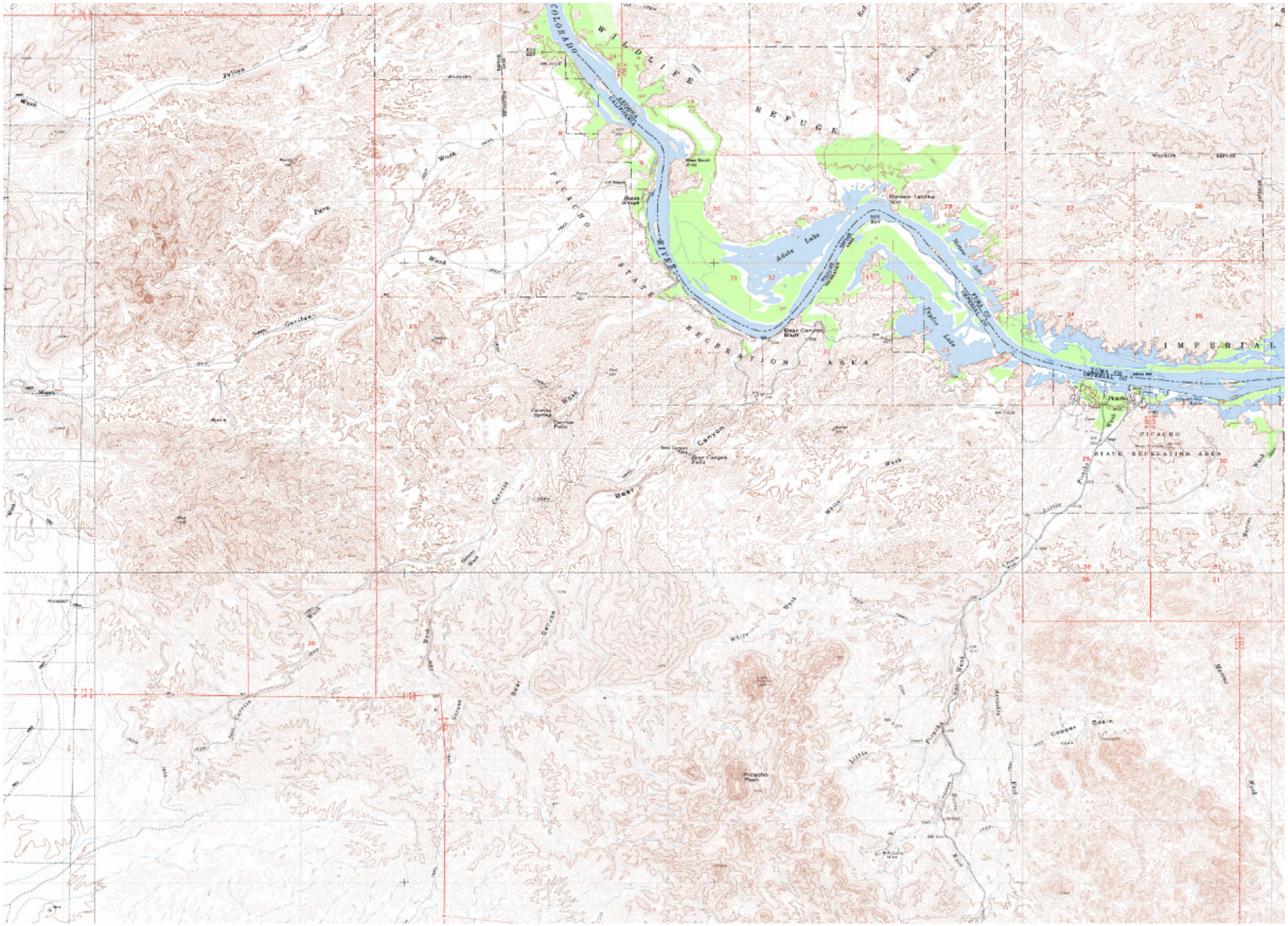

Plate 2. Topographic map used as a base for field mapping. This map is included to provide geographic context to locations mentioned in the text, such as Carrizo Wash, Bear Canyon, PSRA, etc. Other namesakes such as Copper Basin, Sortan Wash, White Wash, and Marcus Wash are also visible on the map. The Colorado River is an easily observable feature in this map and Plate 1.

Tables

Table 1. BCC clast counts and locations used for pie charts in Figures 10 – 12. Os = Orocopia Schist, Mg = mafic orthogneiss, WH = Winterhaven Formation, Volc. = volcanic and epiclastic suite, Cong. = BCC, and Fg = felsic gneiss.

Name	Os	Mg	WH	Volc.	Cong.	Fg	?	*n*	Latitude	Longitude	Grain size counted	Sequence
C1	0	6	0	88	11		0	105			9-0.5 cm	3
C10	0	47	0	39	13	0	0	99			15-2 cm	3
C11	0	0	0	39	4	0	0	43	N 33 0 39.77	W 114 40 56.30	24-1 cm	3
C12	1	59	0	38	1	0	1	100	N 33 0 40.1	W 114 40 46.86	18-1 cm	3
C13	0	0	0	74	26	0	0	100	N 33 0 45.11	W 114 40 36.48	16-1 cm	3
C14	0	0	0	100	0	0	0	100	N 33 0 50.35	W 114 40 28.81	7-1 cm	1
C15	0	0	0	100	0	0	0	100	N 33 0 54.82	W 114 40 21.64	13-2 cm	1
C16	3	39	0	57	0	0	0	99	N 33 1 28.77	W 114 40 11.06	15-1 cm	2
C17	9	62	0	29	0	0	0	100	N 33 1 30.69	W 114 40 3.77	10-1 cm	2
C18	3	48	0	49	0	0	0	100	N 33 1 36.26	W 114 40 2.29	14-1 cm	2
C19	2	45	0	47	5	0	1	100	N 33 1 36.26	W 114 40 2.29	13-1 cm	3
C2	0	5	0	93	1	0	2	101	N 33 0 4.013	W 114 41 22.31	0.1-0.7 cm	3
C20	7	37	0	55	0	0	1	100	N 33 1 43.57	W 114 40 14.73	4-1 cm	3
C21	2	52	0	40	6	0	0	100	N 33 1 43.57	W 114 40 14.73	15-1 cm	3
C22	0	35	0	67	0	0	0	102	N 33 1 50.15	W 114 40 27.73	15-1 cm	3
C23	0	40	0	52	8	0	0	100	N 33 1 43.21	W 114 40 32.97	15-2 cm	3
C24	5	51	0	37	5	0	1	99	N 33 1 55.53	W 114 40 49.70	7-2 cm	3
C25	9	59	0	32	0	0	0	100	N 33 2 4.39	W 114 40 36.84	15-2 cm	2
C26	4	46	0	51	0	0	0	101	N 33 2 19.42	W 114 40 52.36	10-2 cm	2
C27	2	46	0	47	6	0	0	101	N 33 1 33.62	W 114 40 46.95	20-2 cm	3
C28	3	50	0	45	2	0	0	100	N 33 1 14.54	W 114 41 6.60	7-2 cm	3
C29	30	35	0	32	0	0	0	97	N 33 1 35.46	W 114 41 3.48	20-2 cm	2
C3	0	15	0	100	0	0	0	115	N 33 0 6.55	W 114 41 15.28	5.5-0.5 cm	3
C30	0	57	0	32	10	0	1	100	N 33 0 47.42	W 114 41 30.37	13-2 cm	3
C31	20	33	2	45	0	0	0	100	N 33 0 31.52	W 114 41 49.19	18-1 cm	3
C32	0	0	0	100	0	0	0	100	N 33 0 30.48	W 114 41 55.38	8-1 cm	2
C33	15	38	22	25	0	0	0	100	N 33 0 30.48	W 114 41 55.38	8-1 cm	2
C34	9	54	0	37	0	0	0	100	N 33 0 22.64	W 114 41 48.14	18-2 cm	3

Table 1 (continued).

Name	Os	Mg	WH	Volc.	Cong.	Fg	?	*n*	Latitude	Longitude	Grain size counted	Sequence
C35	19	70	11	0	0	0	0	100	N 33 0 6.46	W 114 42 1.91	12-1 cm	3
C36	13	62	19	6	0	0	0	100	N 33 0 6.29	W 114 41 57.14	3.5-0.5 cm	3
C37	10	15	1	66	8	0	0	100	N 33 0 3.62	W 114 41 54.81	23-2 cm	3
C38	32	68	0	0	0	0	0	100	N 32 59 59.04	W 114 42 7.28	9-2 cm	3
C39	11	19	0	68	2	0	0	100	N 32 59 56.10	W 114 42 7.71	10-2 cm	3
C4	0	7	0	74	18	0	2	101	N 33 0 9.64	W 114 41 12.65	12-0.5 cm	3
C40	10	18	0	68	3	0	1	100	N 32 59 36.78	W 114 42 20.75	20-2 cm	3
C41	11	21	0	64	4	0	0	100	N 32 59 33.50	W 114 42 20.87	20-2 cm	3
C42	96	4	0	0	0	0	0	100	N 32 59 24.61	W 114 42 20.43	36-1 cm	3
C43	16	4	0	76	4	0	0	100	N 32 59 29.14	W 114 42 13.33	17-2 cm	3
C44	16	7	0	70	6	0	1	100	N 32 59 39.17	W 114 42 11.08	12-2 cm	3
C45	17	15	0	40	28	0	0	100	N 33 0 14.30	W 114 4 34.26	12-2 cm	3
C46	4	61	0	31	4	0	0	100	N 33 0 19.35	W 114 41 33.40	7-2 cm	3
C47	19	10	0	63	9	0	0	101	N 33 0 21.31	W 114 41 19.41	10-2 cm	3
C48	1	59	1	34	5	0	0	100	N 33 0 46.67	W 114 41 28.44	8-2 cm	3
C49	0	58	0	38	4	0	0	100	N 33 0 50.25	W 114 41 8.53	9-2 cm	3
C5	0	5	0	54	40	0	0	99	N 33 0 12.57	W 114 41 8.67	5-1 cm	3
C50	10	50	2	38	0	0	0	100	N 33 1 21.28	W 114 41 8.55	15-1 cm	2
C51	17	48	1	33	0	0	1	100	N 33 1 51.60	W 114 41 1.00	11-2 cm	2
C52	0	3	0	45	52	0	0	100			9-2 cm	3
C53	0	8	0	28	64	0	0	100	N 33 0 6.13	W 114 40 58.73	15-2 cm	3
C54	1	3	2	57	0	0	0	63	N 32 59 56.81	W 114 41 3.12	9-2 cm	3
C55	4	6	0	42	48	0	0	100	N 32 59 39.02	W 114 41 5.18	4-1 cm	3
C56	14	18	3	31	34	0	0	100	N 32 59 34.08	W 114 41 55.14	6-2 cm	3
C57	7	8	0	73	12	0	0	100	N 32 59 47.81	W 114 41 55.51	8-1 cm	3
C58	1	4	0	77	18	0	0	100	N 32 59 42.21	W 114 41 47.89	8-2 cm	3
C59	0	4	0	93	3	0	0	100	N 32 59 53.83	W 114 41 25.91	10-2 cm	3
C6	3	3	0	59	30	0	0	95	N 33 0 16.54	W 114 41 4.08	7-0.5 cm	3
C60	0	2	0	90	8	0	0	100	N 32 59 45.36	W 114 41 20.43	6-3 cm	3
C61	9	8	0	17	66	0	0	100	N 32 59 35.10	W 114 41 20.79	21-1 cm	3
C62	98	2	0	0	0	0	0	100	N 32 59 35.10	W 114 41 20.79	12-2 cm	3
C63	89	11	0	0	0	0	0	100	N 32 59 26.87	W 114 41 25.43	40-1 cm	3
C64	92	8	0	0	0	0	0	100	N 32 59 24.57	W 114 41 27.16	20-1 cm	3
C65	90	10	0	0	0	0	0	100	N 32 59 17.65	W 114 41 35.97	12-2 cm	3
C66	98	2	0	0	0	0	0	100	N 32 59 9.22	W 114 41 36.08	12-2 cm	3

Table 1 (continued).

Name	Os	Mg	WH	Volc.	Cong.	Fg	?	*n*	Latitude	Longitude	Grain size counted	Sequence
C67	96	4	0	0	0	0	0	100	N 32 58 58.49	W 114 41 39.31	12-2 cm	3
C68	13	87	0	0	0	0	0	100	N 32 58 52.01	W 114 41 23.02	12-2 cm	2
C68.2	2	2	0	96	0	0	0	100	N 32 59 29.31	W 114 40 38.64	8-1 cm	2
C69	0	0	1	99	0	0	0	100	N 32 59 38.48	W 114 40 39.61	8-2 cm	2
C7	1	3	0	59	36	0	1	100			9-1 cm	3
C70	9	34	0	56	0	0	0	99	N 32 59 40.89	W 114 40 39.89	13-1 cm	2
C71	0	13	24	63	0	0	0	100	N 32 59 48.48	W 114 40 23.28	12-1 cm	2
C72	0	11	61	25	0	0	0	97	N 33 0 2.17	W 114 40 38.34	12-0.5 cm	2
C73	2	8	13	77	0	0	0	100	N 33 0 12.70	W 114 40 41.81	6-1 cm	2
C74	1	2	0	93	4	0	0	100	N 33 0 28.30	W 114 40 40.16		3
C75	0	3	0	87	10	0	0	100	N 33 0 40.97	W 114 40 37.69	6-2 cm	3
C76	0	0	0	91	8	0	0	99	N 33 0 35.60	W 114 40 27.92	6-2 cm	3
C77	0	0	0	87	13	0	0	100	N 33 0 27.42	W 114 40 26.95	5-1 cm	3
C78	0	0	0	90	9	0	0	99	N 33 0 21.52	W 114 40 21.47	5-1 cm	3
C79	0	8	33	59	0	0	0	100	N 33 0 7.38	W 114 40 21.64	12-1 cm	2
C8	0	2	0	58	40	0	0	100			6-0.5 cm	3
C80	0	5	44	37	0	0	0	86	N 33 0 4.45	W 114 40 17.46	7-0.5 cm	2
C81	0	11	51	38	0	0	0	100	N 32 59 55.51	W 114 40 7.44	5-0.5 cm	2
C82	0	10	49	41	0	0	0	100	N 32 59 47.81	W 114 40 6.21	15-0.5 cm	2
C83	0	7	52	41	0	0	0	100	N 32 59 40.76	W 114 40 6.29	7-1 cm	2
C84	0	0	0	100	0	0	0	100	N 32 59 35.87	W 114 40 4.13	14-1 cm	2
C85	0	4	0	36	60	0	0	100	N 32 59 35.87	W 114 40 4.13	9-1 cm	3
C86	11	13	35	41	0	0	0	100	N 32 59 36.84	W 114 39 57.45	6-1 cm	2
C87	0	0	0	99	0	0	1	100	N 32 59 34.97	W 114 39 54.48	12-2 cm	2
C88	0	0	0	100	0	0	0	100	N 32 59 31.91	W 114 39 36.02	7-1 cm	2
C89	43	74	0	0	0	0	0	117	N 32.981345	W 114.701279	150-5 cm	2
C9	6	54	0	40	3	0	0	103			<1 cm	3
C90	22	14	29	34	5	0	0	104	N 32.981345	W 114.701279	20-2 cm	3
C91	34	13	7	45	1	0	0	100	N 32.997124	W 114.716378	10-2 cm	3
C92	75	2	3	20	0	0	0	100	N 32.995219	W 114.721130	15-2 cm	3
C93	55	45	0	0	0	0	0	100	N 32.985953	W 114.708923	100-2 cm	2
C94	28	10	11	51	0	0	0	100	N 32.983752	W 114.719791	40-2 cm	2
C95	1	123	0	10	0	0	0	134	N 32.984178	W 114.742470	20-2 cm	3
C96	36	10	7	49	0	0	0	102	N 32.987504	W 114.741205	18-2 cm	3
C97	1	0	0	10	0	123	0	134	N 32.984178	W 114.742470	14-2 cm	3

Table 2. Locations and clast count sizes used for Figure 12.

Name	Latitude	Longitude	Max. BCC clast size (cm)
305	N 33 0 33.61	W 114 41 12.60	43
312	N 33 0 48.92	W 114 40 36.81	80
313	N 33 0 41.38	W 114 40 41.76	110
314	N 33 0 39.72	W 114 40 57.08	300
316	N 33 0 25.62	W 114 41 4.60	70
317	N 33 0 14.31	W 114 41 6.02	160
318	N 32 59 49.60	W 114 41 24.02	37
319	N 32 59 27.92	W 114 41 24.66	110
320	N 32 59 36.68	W 114 41 55.31	75
323	N 33 0 53.34	W 114 41 9.38	24
324	N 33 0 23.90	W 114 41 7.37	69
325	N 33 0 21.31	W 114 41 19.41	68
326	N 33 0 14.30	W 114 41 31.53	39
329	N 32 59 29.39	W 114 42 5.34	13
333	N 31 59 34.92	W 114 39 38.65	100
338	N 33 1 54.95	W 114 40 24.21	37
339	N 33 1 42.29	W 114 40 29.15	80
340	N 33 1 28.46	W 114 40 10.46	35
341	N 33 1 36.26	W 114 40 2.29	52
342	N 33 1 24.09	W 114 40 27.61	58
343	N 33 1 14.84	W 114 40 30.94	93
346	N 33 0 3.28	W 114 41 55.10	90
347	N 33 1 26.43	W 114 41 31.20	22
348	N 33 2 0.83	W 114 40 35.00	130
350			90
351	N 32 59 43.03	W 114 41 30.08	37

Table 3. Planar data of each fault measured with rake. This data was used to determine slip sense and to make Figures 14 – 16.

Name	Strike	Dip	Note	Plane type	Rake	Slip sense
1	10	82	Reidel shears	fault	14 S	right lateral
2	232	65	Reidel shears, strike-slip	fault	22 S	right lateral
3	187	84	Reidel shears	fault		right lateral
4	193	86	Reidel shears	fault		right lateral
5	156	45	dip-slip	fault	85 N	normal
6	16	78	Reidel shears	fault		right lateral
7	96	65	Winterhaven faulted on top of gneiss clast breccia	fault		reverse
8	110	49		fault		reverse
9	164	62	dip-slip	fault	87 S	normal
10	344	75	oblique	fault	45 N	reverse
11	110	30		fault		reverse
12	175	40	dip-slip	fault	85 N	normal
13	181	80	dip-slip, rake 15 N (less prominent)	fault	60 N	normal
14	345	75	dip-slip	fault	78 N	normal
15	175	74	dip-slip	fault	80 S	normal
16	344	77	dip-slip	fault	65 N	normal
17	355	81	strike-slip	fault	18 S	?
18	166	65	dip-slip	fault	54 N	normal
19	175	72	dip-slip	fault	84 N	normal
20	340	88	strike-slip	fault	12 S	right lateral
21	245	75	strike-slip	fault	10 N	left lateral

Vita

Garrett Goff was born in Indianapolis, Indiana. After high school he attended and swam for Olivet Nazarene University for a year before transferring to Indiana University Purdue University – Indianapolis (IUPUI) to continue his swimming career. He was a two-time Summit League Top 8 finisher and a captain for his team. While at IUPUI, he studied the geochemical differences in intrusive and extrusive rocks and zircons in the Sierra Nevada batholith with Dr. Andrew Barth, and he gave a poster presentation on this topic at the GSA Spring 2016 meeting in Denver. In August 2017 he graduated from IUPUI with his Bachelor of Science in Geological Sciences.

Immediately after this he moved to El Paso to pursue his Master of Science in Geology at The University of Texas at El Paso (UTEP). Here he studied the syndepositional tectonics of the Bear Canyon Conglomerate with Dr. Jason Ricketts. While attending UTEP he served in student chapters of national organizations as vice president of the Society of Economic Geologists (SEG) and secretary of the American Association of Petroleum Geologists (AAPG). He also served on the organizing committee of the UTEP Geological Sciences Colloquium in 2018 and 2019 and was a member of Sigma Gamma Epsilon/UTEP Geology Club during the same years.

After graduating with his Master of Science, Garrett plans to begin working as a GIS analyst in the environmental sector.3

This thesis was typed by the author, Garrett Goff.

Contact information: iamgarrettgoff@gmail.com